6 Stellar Populations in the Milky Way and Nearby Galaxies

Abhijit Saha, Kevin R. Covey, Timothy C. Beers, John J. Bochanski, Pat Boeshaar, Adam J. Burgasser, Phillip A. Cargile, You-Hua Chu, Charles F. Claver, Kem H. Cook, Saurav Dhital, Laurent Eyer, Suzanne L. Hawley, Leslie Hebb, Eric J. Hilton, J. B. Holberg, Željko Ivezić, Mario Jurić, Jason Kalirai, Sébastien Lépine, Lucas M. Macri, Peregrine M. McGehee, David Monet, Knut Olsen, Edward W. Olszewski, Joshua Pepper, Andrej Prša, Ata Sarajedini, Sarah Schmidt, Keivan G. Stassun, Paul Thorman, Andrew A. West, Benjamin F. Williams

6.1 Introduction

Stellar populations, consisting of individual stars that share coherent spatial, kinematic, chemical, or age distributions, are powerful probes of a wide range of astrophysical phenomena. The coherent properties of stellar populations allow us to use measurements of an individual member to inform our understanding of the larger system and vice versa. As examples, globular cluster metallicities are often derived from measurements of the brightest few members, while the overall shape of the cluster color magnitude diagram (CMD) enables us to assign ages to an individual star within the system. Leveraging the wealth of information available from such analyses enables us to develop a remarkably detailed and nuanced understanding of these complex stellar systems.

By providing deep, homogeneous photometry for billions of stars in our own Galaxy and throughout the Local Group, LSST will produce major advances in our understanding of stellar populations. In the sections that follow, we describe how LSST will improve our understanding of stellar populations in external galaxies (§ 6.2 and § 6.3) and in our own Milky Way (§§ 6.4–6.6), and will allow us to study the properties of rare stellar systems (§§ 6.7–6.11).

Many of the science cases in this chapter are based on the rich characterization LSST will provide for stars in the solar neighborhood. This scientific landscape will be irrevocably altered by the Gaia space mission, however, which will provide an exquisitely detailed catalog of millions of solar neighborhood stars shortly after its launch (expected in 2011). To illuminate the scientific areas where LSST provides a strong complement to Gaia's superb capabilities, § 6.12 develops a quantitative comparison of the astrometric and photometric precision of the two missions; this comparison highlights LSSTs ability to smoothly extend Gaia's solar neighborhood catalog to redder targets and fainter magnitudes.

6.2 The Magellanic Clouds and their Environs

Abhijit Saha, Edward W. Olszewski, Knut Olsen, Kem H. Cook

The Large and Small Magellanic Clouds (LMC and SMC respectively; collectively referred to hereafter as "the Clouds") are laboratories for studying a large assortment of topics, ranging from stellar astrophysics to cosmology. Their proximity allows the study of their individual constituent stars: LSST will permit broad band photometric "static" analysis to $M_V \sim +8$ mag, probing well into the M dwarfs; and variable phenomena to $M_V \sim +6$, which will track main sequence stars 2 magnitudes fainter than the turn-offs for the oldest known systems.

A sense of scale on the sky is given by the estimate of "tidal debris" extending to 14 kpc from the LMC center (Weinberg & Nikolaev 2001) based on 2MASS survey data. Newer empirical data (discussed below) confirm such spatial scales. The stellar bridge between the LMC and SMC is also well established. Studies of the full spatial extent of the clouds thus require a wide area investigation of the order of 1000 deg^2. We show below that several science applications call for reaching "static" magnitudes to V or $g \approx 27$ mag, and time domain data and proper motions reaching 24 mag or fainter. The relevance of LSST for these investigations is unquestionable.

Nominal LSST exposures will saturate on stars about a magnitude brighter than the horizontal branch luminosities of these objects, and work on such stars is not considered to be an LSST forte. Variability surveys like MACHO and SuperMACHO have already covered much ground on time-domain studies, with SkyMapper to come between now and LSST. We do not consider topics dealing with stars bright enough to saturate in nominal LSST exposures.

6.2.1 Stellar Astrophysics in the Magellanic Clouds

For stellar astrophysics studies, the Clouds present a sample of stars that are, to first order, at a common distance, but contain the complexity of differing ages and metallicities, and hence an assortment of objects that star clusters within the Galaxy do not have. In addition, the age-metallicity correlation in the Clouds is known to be markedly different from that in the Galaxy. This allows some of the degeneracies in stellar parameters that are present in Galactic stellar samples to be broken.

LSST's extended time sampling will reveal, among other things, eclipsing binaries on the main sequence through the turn-off. We plan to use them to calibrate the masses of stars near the old main sequence turnoff. Only a small number of such objects are known in our own Galaxy, but wide area coverage of the Clouds (and their extended structures) promises a sample of $\sim 80,000$ such objects with $22 < g < 23$ mag, based on projections from MACHO and SuperMACHO. Binaries in this brightness range track evolutionary phases from the main sequence through turn-off. The direct determination of stellar masses (using follow-up spectroscopy of eclipsing binaries identified by LSST) of a select sub-sample of eclipsing binaries in this range of evolutionary phase will confront stellar evolution models, and especially examine and refine the stellar age "clock," which has cosmological implications.

For this question, we need to determine the number of eclipsing binaries (EB) that LSST can detect within 0.5 magnitudes of the old turn-off ($r \sim 22.5$). Additionally, because the binary mass depends on $(\sin i)^3$, we need to restrict the EB sample to those with $i = 90° \pm 10°$ in order to determine masses to 5%. Such accuracy in mass is required for age sensitivity of $\sim$ 2 Gyr at ages of 10-12 Gyr. We determined the number of LMC EBs meeting these restrictions that could be discovered by LSST by projecting from the 4631 eclipsing binaries discovered by the MACHO project (e.g. Alcock et al. 1995). Selecting only those MACHO EBs with colors placing them on the LMC main sequence, we calculated the minimum periods which these binaries would need to have in order for them to have inclinations constrained to be $90° \pm 10°$, given their masses and radii on the main sequence. Of the MACHO EB sample, 551 systems (12%) had periods longer than the minimum, with the majority of the EBs being short-period binaries with possibly large inclinations. Next, we constructed a deep empirical LMC stellar luminosity function (LF) by combining the V-band luminosity function from the Magellanic Clouds Photometric Survey (Zaritsky et al. 2004, MCPS) with the HST-based LMC LF measured by Dolphin (2002a), using Smecker-Hane et al. (2002) observations of the LMC bar, where we scaled the HST LF to match the MCPS LF over the magnitude range where the LFs overlapped. We then compared this combined LF to the LF of the MACHO EBs, finding that EBs comprise $\sim$ 2% of LMC stellar sources. Finally, we used our deep combined LF to measure the number of LMC stars with $22 < V < 23$, multiplied this number by 0.0024 to account for the fraction of sufficiently long-period EBs, and found that LSST should be able to detect $\sim 80,000$ EBs near the old main sequence turnoff. Based on the MACHO sample, these EBs will have periods between $\sim$ 3 and $\sim$ 90 days, with an average of $\sim$ 8 days.

LSST is expected to find $\sim 10^5$ RR Lyrae stars over the full face of both Clouds (the specific ratio of RR Lyraes can vary by a factor of 100, and the above estimate, which is based on 1 RR Lyrae per $\sim 10^4 L_\odot$, represents the geometric mean of that range and holds for HST discoveries of RR Lyrae stars in M31 and for SuperMACHO results in the Clouds). The physics behind the range of subtler properties of RR Lyrae stars is still being pondered: trends in their period distributions as well as possible variations in absolute magnitude with period, age, and metallicity. Our empirical knowledge of these comes from studying their properties in globular clusters, where the distance determinations may not be precise enough (at the 20% level). The range of distances within the LMC is smaller than the uncertainty in relative distances between globular clusters in our Galaxy. Ages and metallicities of the oldest stars (the parent population of the RR Lyraes) in any given location in the Clouds may be gleaned from an analysis of the local color-magnitude diagrams, as we now discuss, and trends in RR Lyrae properties with parent population will be directly mapped for the first time.

6.2.2 The Magellanic Clouds as "Two-off" Case Studies of Galaxy Evolution

The Clouds are the only systems larger and more complex than dwarf spheroidals outside our own Galaxy where we can reach the main sequence stars with LSST. Not only are these the most numerous, and therefore the most sensitive tracers of structure, but they *proportionally represent stars of all ages and metallicities*. Analyzing the ages, metallicities, and motions of these stars is the most effective and least biased way of parsing the stellar sub-systems within any galaxy, and the route to understanding the history of star formation, accretion, and chemical evolution of the galaxy as a whole. Decades of work toward this end have been carried out to define these elements within our Galaxy, but the continuing task is made difficult not only because of the vastness on the sky, but also because determining distances to individual stars is not straightforward. The Clouds are the *only* sufficiently complex systems (for the purpose of understanding galaxy assembly) where the spatial perspective allows us to know where in the galaxy the stars we are examining lie, while at the same time being close enough for us to examine and parse its component stellar populations in an unbiased way through the main sequence stars. LSST will provide proper motions of individual stars to an accuracy of $\sim 50 \mathrm{km\,s^{-1}}$ in the LMC, but local ensembles of thousands of stars on spatial scales from 0.1 to several degrees will be able to separate disk rotation from a "stationary" halo. Internal motions have been seen using proper motions measured with only 20 positional pointings with the HST's Advanced Camera for Surveys (ACS) with only a few arc-min field of view and a 2-3 year time baseline (Piatek et al. 2008).

Color-magnitude and Hess diagrams from a composite stellar census can be decomposed effectively using stellar evolution models (e.g., Tolstoy & Saha 1996; Dolphin 2002b). While the halo of our Galaxy bears its oldest *known* stars, models of galaxy formation lead us to expect the oldest stars to live in the central halo and bulge. Age dating the oldest stars toward the center of the Galaxy is thwarted by distance uncertainties, complicated further by reddening and extinction. The Clouds present objects at a known distance, where color-magnitude diagrams are a sensitive tool for evaluating ages. A panoramic unbiased age distribution map from the CMD turn-off is not possible at distances larger than 100 kpc. The Clouds are a gift in this regard.

6.2.3 The Extended Structure of the Magellanic Clouds

Knowledge of the distribution and population characteristics in outlying regions of the LMC/SMC complex is essential for understanding the early history of these objects and their place in the ΛCDM hierarchy. In our Galaxy the most metal poor, and (plausibly) the oldest observed stars are distributed in a halo that extends beyond 25 kpc. Their spatial distribution, chemical composition and kinematics provide clues about the Milky Way's early history, as well as its continued interaction with neighboring galaxies. If the Clouds also have similar halos, the history of their formation and interactions must also be written in their stars. In general how old are the stars in the extremities of the Clouds? How are they distributed (disk or halo dominated)? How far do such stellar distributions extend? What tidal structure is revealed? Is there a continuity in the stellar distribution between the LMC and SMC? Do they share a common halo with the Galaxy? What do the kinematics of stars in outlying regions tell us about the dark matter distribution? Is there a smooth change from disk to non-disk near the extremities?

Past panoramic studies such as with 2MASS and DENIS have taught us about the LMC disk *interior* to 9 kpc (10°, e.g., van der Marel 2001). Structure beyond that had not been systematically probed in an *unbiased* way (studies using HII regions, carbon stars, and even RR Lyrae exist, but they are heavily biased in age and metallicity) until a recent pilot study (NOAO Magellanic Outer Limits Survey) with the MOSAIC imager on the Blanco 4-m telescope at Cerro Tololo Inter-American Observatory, which uses main sequence stars as tracers of structure. Even with their very selective spatial sampling of a total of only $\sim 15\ \mathrm{deg}^2$ spread out over a region of interest covering over $\sim 1000\ \mathrm{deg}^2$, the LMC disk is seen to continue out to 10 disk scale lengths, beyond which there are signs either of a spheroidal halo that finally overtakes the disk (a simple scaled model of how our own Galaxy must look when viewed face on), or a tidal pile-up. Main sequence stars clearly associated with the LMC are seen out to 15 degrees along the plane of the disk (Figure 6.1). This exceeds the tidal radius estimate of 11 kpc (12.6°) by Weinberg (2000), already

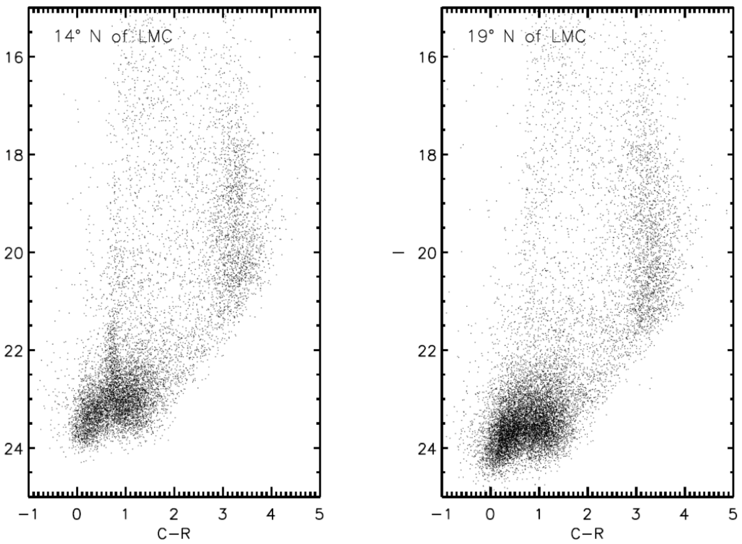

Figure 6.1: The color-magnitude diagrams in $C - R$ vs. R for two fields, 14° (left) and 19° (right) due north of the LMC center. The stub-like locus of stars near $C - R \sim 0.7$ and $I > 21.0$ that can be seen on the left panel for the 14° field corresponds to the locus of old main sequence stars from the LMC, which have a turn-off at $I \sim 21.0$. This shows that stars associated with LMC extend past 10 disk scale lengths. The feature is absent in the 19° field, which is farther out. Mapping the full extent of the region surrounding the Clouds on these angular scales is only feasible with LSST.

a challenge to existing models of how the LMC has interacted with the Galaxy. (This extended LMC structure has a surface brightness density of ~ 35 mag per square arc-sec, which underscores the importance of the Clouds and the opportunity they present, because this technique will not work for objects beyond 100 kpc from us.) In contrast, the structure of the SMC appears to be very truncated, at least as projected on the sky. Age and metallicity of these tracer stars are also derived in straightforward manner.

Not only will LSST map the complete extended stellar distribution (where currently less than 1% of the sky region of interest has been mapped) of the Clouds using main sequence stars as tracers that are unbiased in age and metallicity, but it will also furnish proper motions. The accuracy of ensemble average values for mapping streaming motions, such as disk rotation and tidal streams, depends eventually on the availability of background quasars and galaxies, which do not move on the sky. The HST study of proper motions (Kallivayalil et al. 2006b,a; Piatek et al. 2008) was able to use quasars with a surface density of 0.7 deg^{-2}. We expect that LSST, using the hugely more numerous background galaxies as the “zero proper motion reference,” and a longer time baseline should do even better. Individual proper motions of stars at these distances can be measured to no better than ~ 50 km s^{-1}, but the group motions of stars will be determined to much higher accuracy, depending ultimately on the positional accuracy attainable with background galaxies. Over scales of 0.1°, statistical analysis of group motions can be expected to yield systemic motions with accuracies better than 10 km s^{-1}. This would not only discriminate between disk and halo components of the Clouds in their outer regions but also identify any tidally induced structures at their extremities.

6.2.4 The Magellanic Clouds as Interacting Systems

In addition to interacting gravitationally with each other, both Clouds are in the gravitational proximity of the Galaxy. Until recently, it was held that the Clouds are captive satellites of the Galaxy and have made several passages through the Galaxy disk. The extended stream of HI, called the Magellanic Stream, which emanates from near the SMC and wraps around much of the sky, has been believed to be either a tidal stream or stripped by ram pressure from passages through the Galaxy disk. This picture has been challenged recently by new proper motion measurements in the Clouds from HST data analyzed by two independent sets of investigators (Kallivayalil et al. 2006b,a; Piatek et al. 2008). Their results indicate significantly higher proper motions for both systems, which in turn imply higher space velocities. Specifically, the LMC and SMC may not have begun bound to one another, and both may be on their first approach to the Milky Way, not already bound to it. Attempts to model the motion of the Clouds together with a formation model for the Magellanic Stream in light of the new data (e.g., Besla et al. 2009) are very much works in progress. Even if a higher mass sufficient to bind the Clouds is assumed for the Galaxy, the orbits of the Clouds are changed radically from prior models: specifically, the last peri-galacticon could not have occurred within the last 5 Gyrs with the high eccentricity orbits that are now necessary (Besla et al. 2009), indicating that the Magellanic Stream cannot be tidal. The proper motion analyses have also determined the rotation speed of the LMC disk (Piatek et al. 2008). The new result of $120 \pm 15\,\mathrm{kms}^{-1}$ is more reliable than older radial velocity-based estimates for this nearly face-on galaxy, and as much as twice as large as some of the older estimates. This new scenario changes the expected tidal structures for the Clouds and argues against a tidal origin for the Magellanic Stream. These expectations are empirically testable with LSST. For instance, a tidal origin requires a corresponding stream of stars, even though the stellar stream can be spatially displaced with respect to the gas stream: to date, such a star stream, if its exists, has escaped detection. A definitive conclusion about whether such a stellar stream exists or not, awaits a deep multi-band wide area search to detect and track main sequence stars, which are the most sensitive tracers of such a stellar stream.

Aside from the specific issue of a stellar stream corresponding to the Magellanic gas stream, the full area mapping of extremities via the main sequence stars described in § 6.2.3 will reveal any tidally induced asymmetries in the stellar distributions, e.g., in the shape of the LMC disk as result of the Galactic potential as well as from interaction with the SMC. Proper motions of any tidal debris (see § 6.2.3) will contribute to determining the gravitational field, and eventually to a modeling of the halo mass of the Galaxy. How far out organized structure in the LMC persists, using kinematic measures from proper motions, will yield the mass of the LMC, and thus the size of its dark matter halo.

6.2.5 Recent and On-going Star Formation in the LMC

You-Hua Chu

Studies of recent star formation rate and history are complicated by the mass dependence of the contraction timescale. For example, at $t \sim 10^5$ yr, even O stars are still enshrouded by circumstellar dust; at $t \sim 10^6$ yr, massive stars have formed but intermediate-mass stars have not reached the

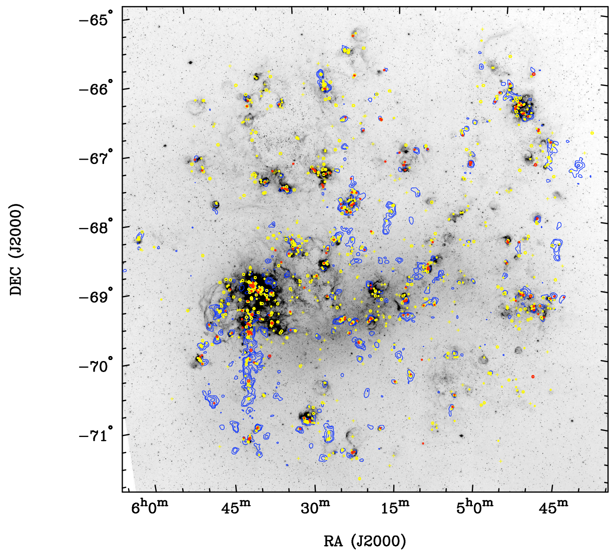

Figure 6.2: Hα image of the LMC. CO contours extracted from the NANTEN survey are plotted in blue to show the molecular clouds. Young stellar objects with 8.0 μm magnitude brighter than 8.0 are plotted in red, and the fainter ones in yellow. Roughly, the brighter objects are of high masses and the fainter ones of intermediate masses. Adapted from Gruendl & Chu (2009).

main sequence; at $t \sim 10^7$ yr, the massive stars have already exploded as supernovae, but the low-mass stars are still on their way to the main sequence.

The current star formation rate in the LMC has been determined by assuming a Salpeter initial mass function (IMF) and scaling it to provide the ionizing flux required by the observed Hα luminosities of HII regions (Kennicutt & Hodge 1986). Individual massive stars in OB associations and in the field have been studied photometrically and spectroscopically to determine the IMF, and it has been shown that the massive end of the IMF is flatter in OB associations than in the field (Massey et al. 1995).

The Spitzer Space Telescope has allowed the identification of high- and intermediate-mass young stellar objects (YSOs), representing ongoing (within 10^5 yr) star formation, in the LMC (Caulet et al. 2008; Chen et al. 2009). Using the Spitzer Legacy program SAGE survey of the central $7° \times 7°$ area of the LMC with both IRAC and MIPS, YSOs with masses greater than $\sim 4\,M_\odot$ have been identified independently by Whitney et al. (2008) and Gruendl & Chu (2009). Figure 6.2 shows the distribution of YSOs, HII regions, and molecular clouds, which represent sites of on-going, recent, and future star formation respectively. It is now possible to fully specify the formation of massive stars in the LMC.

The formation of intermediate- and low-mass stars in the LMC has begun to be studied only recently by identifying pre-main sequence (PMS) stars in $(V - I)$ vs V color-magnitude diagrams (CMDs), as illustrated in Figure 6.3. Using HST WFPC2 observations, low-mass main sequence stars in two OB associations and in the field have been analyzed to construct IMFs, and different slopes are also seen (Gouliermis et al. 2006a,b, 2007).

Using existing HST image data in LMC molecular clouds to estimate how crowding will limit

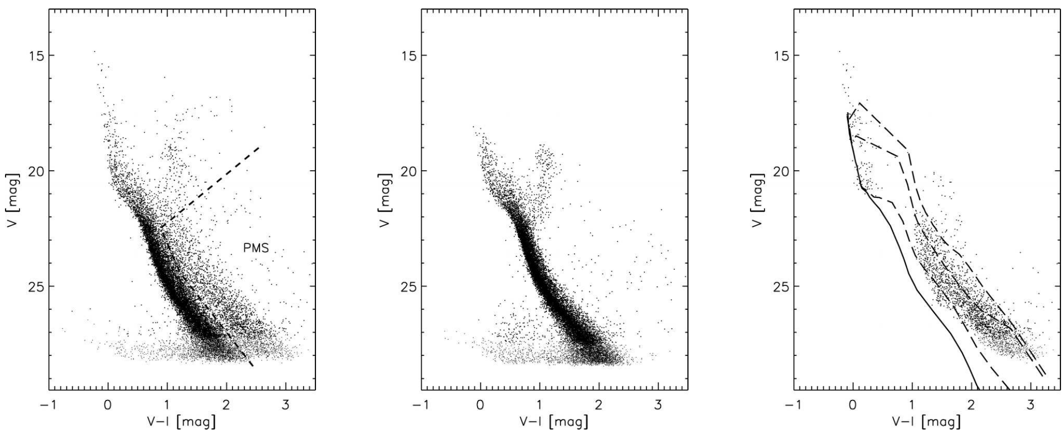

Figure 6.3: V-I vs. V color-magnitude diagram of stars detected in the OB association LH95 (left), surrounding background region (middle), and the difference between the two (right). The zero-age main sequence is plotted as a solid line, and PMS isochrones for ages 0.5, 1.5, and 10 Myr are plotted in dashed lines in the right panel. Adapted from Gouliermis et al. (2007) with permission.

photometry from LSST images, we estimate that PMS stars can be detected down to 0.7-0.8 $M_{\odot}$ ($g \sim 24$ mag: see right hand panel of Figure 6.3). LSST will provide a mapping of intermediate- to low-mass PMS stars in the entire LMC except the bar, where crowding will prevent reliable photometry at these magnitudes. This young lower-mass stellar population, combined with the known information on massive star formation and distribution/conditions of the interstellar medium (ISM), will allow us to fully characterize the star formation process and provide critical tests to different theories of star formation.

Conventionally, star formation is thought to start with the collapse of a molecular cloud that is gravitationally unstable. Recent models of turbulent ISM predict that colliding HI clouds can also be compressed and cooled to form stars. Thus, both the neutral atomic and molecular components of the ISM need to be considered in star formation. The neutral atomic and molecular gas in the LMC have been well surveyed: the ATCA+Parkes map of HI (Kim et al. 2003), the NANTEN survey of CO (Fukui et al. 2008), and the MAGNA survey of CO (Ott et al. 2008, Hughes et al., in prep.). Figure 6.2 shows that not all molecular clouds are forming massive stars: How about intermediate- and low-mass stars? Do some molecular clouds form only low-mass stars? Do stars form in regions with high HI column density but no molecular clouds? These questions cannot be answered until LSST has made a complete mapping of intermediate- and low-mass PMS stars in the LMC.

6.3 Stars in Nearby Galaxies

Benjamin F. Williams, Knut Olsen, Abhijit Saha

6.3.1 Star Formation Histories

General Concepts

Bright individual stars can be distinguished in nearby galaxies with ground-based observations. In galaxies with no recent star formation (within ~1 Gyr), the brightest stars are those on the asymptotic giant branch (AGB) and/or the red giant branch (RGB). The color of the RGB depends mostly on metallicity, and only weakly on age, whereas the relative presence and luminosity distribution of the AGB stars is sensitive to the star formation history in the range $2 < t < 8$ Gyrs. The brightest RGB stars are at $I \sim -4$, and in principle are thus visible to LSST out to distances ~ 10 Mpc. The presence of significant numbers of RR Lyrae stars indicates an ancient population of stars, 10 Gyrs or older. RR Lyrae, as well the brightest RGB stars, are standard candles that measure the distance of the host galaxy.

In practice, object crowding at such distances is severe for galaxies of any significant size, and resolution of individual RGB stars in galaxies with $M_V \sim -10$ and higher will be limited to distances of ~ 4 Mpc, but that includes the Sculptor Group and the Centaurus and M83 groups. Within the Local Group, the "stacked" photometry of individual stars with LSST will reach below the Horizontal Branch, and certainly allow the detection of RR Lyraes in addition to the RGB.

Galaxies that have made stars within the last 1 Gyrs or so contain luminous supergiant stars (both blue and red). The luminosity distributions of these stars reflect the history of star formation within the last 1 Gyr. The brightest stars (in the youngest systems) can reach $M_V \sim -8$, but even stars at $M_V \sim -6$ (including Cepheids) will stand out above the crowding in LSST images of galaxies at distances of ~ 7 Mpc.

A great deal of work along these lines is already being done, both from space and the ground. LSST's role here will be to (1) cover extended structures, and compare, for example, how populations change with location in the galaxies – important clues to how galaxies were formed, and (2) identify the brighter variables, such as RR Lyraes, Cepheids, and the brighter eclipsing binaries wherever they are reachable.

Methods and Techniques

Methods of deriving star formation histories (the distribution of star formation rate as a function of time and chemical composition) from Hess diagrams given photometry and star counts in two or more bands (and comparing with synthetic models) are adequately developed, e.g., Dolphin (2002b). For extragalactic systems and in the solar neighborhood, where distances are known independently, the six-band LSST data can be used to self-consistently solve for extinction and star formation history. This is more complicated if distances are not known independently, such as within the Galaxy, where other methods must be brought to bear. For nearby galaxies, distances are known at least from the bright termination of the RGB.

Analysis of a composite population, as observed in a nearby galaxy, is performed through detailed fitting of stellar evolution models to observed CMDs. An example CMD of approximately LSST depth is shown in Figure 6.4, along with an example model fit and residuals using the stellar evolution models of Girardi et al. (2002) and Marigo et al. (2008). The age and metallicity distribution from this fit are shown in Figure 6.5. These kinds of measurements can show how star formation has progressed within a galaxy over the past Gyr (e.g. Dohm-Palmer et al. 2002; Williams 2003), and provides the possibility of looking for radial trends that provide clues about galaxy formation.

This work requires obtaining as much information as possible about the completeness and photometric errors as a function of position, color, and magnitude. The most reliable way to determine these values is through artificial star tests in which a point spread function typical of the LSST seeing at the time of the each observation is added to the LSST data, and then the photometry of the region is remeasured to determine 1) if the fake star was recovered and 2) the difference between the input and output magnitude. This action must be performed millions of times to get a good sampling of the completeness and errors over the full range in color and magnitude over reasonably small spatial scales. Furthermore, extinction in the field as a function of position must be well-characterized, which requires filters that are separated by the Balmer break. The LSST u filter fits the bill nicely.

In order to be able to perform detailed studies of the age and metallicity distribution of stars in the LSST data, we will need to add artificial stars to the data to test our completeness. We will also need a reliable model for foreground Galactic contamination, because the halos of nearby galaxies may be sparsely populated and contain stars with colors and apparent magnitudes similar to those of the Galactic disk and halo.

6.4 Improving the Variable Star Distance Ladder

Lucas M. Macri, Kem H. Cook, Abhijit Saha, Ata Sarajedini

Pulsating variable stars such as Cepheids and RR Lyraes have been indispensable in the quest to understand the scale of the Universe. The Cepheid Period-Luminosity-Color relation has been long established and used initially to determine the distance to the Large Magellanic Cloud, and then to our nearest spiral neighbor M31. Their shorter period and fainter cousins, the RR Lyraes, are ubiquitous in globular clusters and among the field star population; they can also be used in a relatively straightforward manner to measure distances.

6.4.1 Cepheids and Long Period Variables

There is a major scientific interest in the use of Cepheid variables to calibrate the absolute luminosity of type Ia supernovae (SNe) and other cosmological distance indicators like the Tully-Fisher relation, leading to improved determination of the Hubble constant (H_0). The discovery of dark energy a decade ago brought new attention to this topic because an increase in the precision of the measurement of H_0 results in a significant reduction of the uncertainty in w, the parameter that describes the equation of state of dark energy (Appendix A).

Current efforts are aimed at measuring H_0 with a precision of 5% or better, through a robust and compact distance ladder that starts with a maser distance to NGC 4258. Next comes the discovery of Cepheids in that galaxy using optical data (acquired with HST, Gemini, and LBT), which is followed up in the near-infrared with HST to establish a NIR period-luminosity relation that is accurately calibrated in terms of absolute luminosity and exhibits small scatter. Lastly,

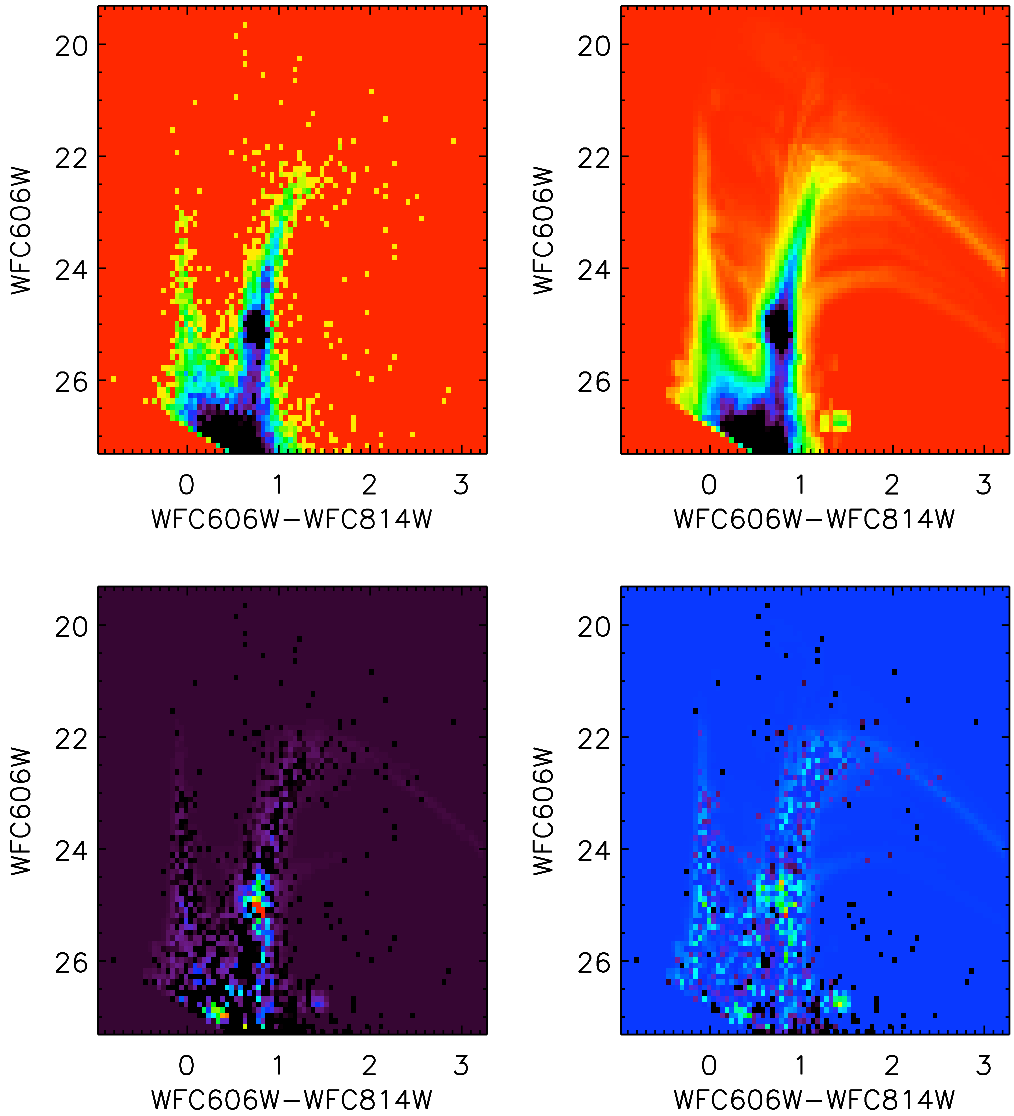

Figure 6.4: Best fit to a CMD from an archival Hubble Space Telescope Advanced Camera for Surveys field in M33. *Upper left:* The observed CMD. *Upper right:* The best-fitting model CMD using stellar evolution models. *Lower left:* The residual CMD. Redder colors denote an overproduction of model stars. Bluer colors denote an underproduction of model stars. *Lower right:* The deviations shown in *lower left* normalized by the Poisson error in each CMD bin, i.e., the statistical significance of the residuals. Only the red clump shows statistically significant residuals.

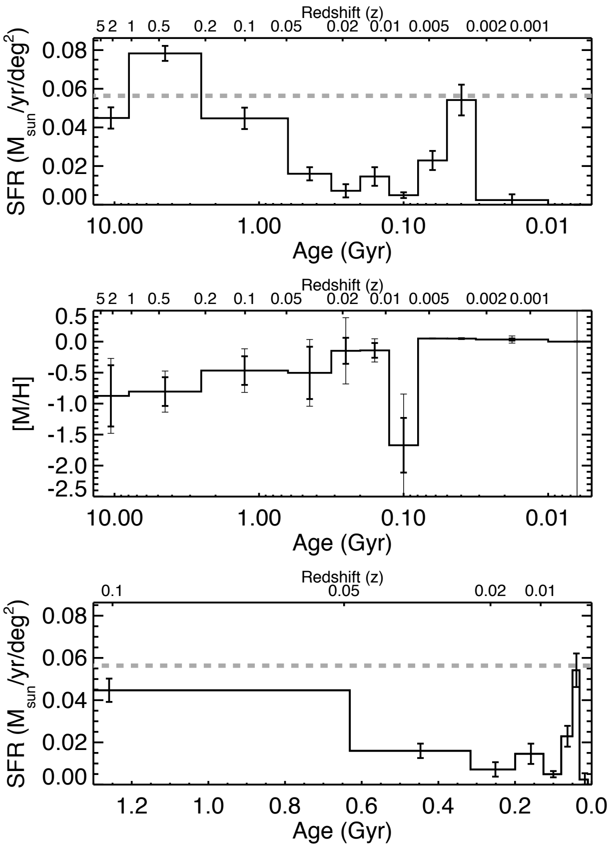

Figure 6.5: The star formation history from the CMD shown in Figure 6.4. *Top:* The solid histogram marks the star formation rate (normalized by sky area) as a function of time for the past 14 Gyr. The dashed line marks the best-fitting constant star formation rate model. *Middle:* The mean metallicity and metallicity range of the population as a function of time. Heavy error bars mark the measured metallicity range, and lighter error bars mark how that range can slide because of errors in the mean metallicity. *Bottom:* Same as *top*, but showing only the results for the past 1.3 Gyr.

Cepheids are discovered in galaxies that were hosts to modern type Ia SNe to calibrate the absolute luminosity of these events and determine H_0 from observations of SNe in the Hubble flow.

In the next few years before LSST becomes operational, we anticipate using HST and the ladder described above to improve the precision in the measurement of H_0 to perhaps 3%. Any further progress will require significant improvement in several areas, and LSST will be able to contribute significantly to these goals as described below.

- We need to address the intrinsic variation of Cepheid properties from galaxy to galaxy. This can only be addressed by obtaining large, homogeneous samples of variables in many galaxies. LSST will be able to do this for all southern spirals within 8 Mpc.
- We need to calibrate the absolute luminosity of type Ia SNe more robustly, by increasing the number of host galaxies that have reliable distances. Unfortunately HST cannot discover Cepheids (with an economical use of orbits) much further out than 40 Mpc, and its

days are numbered. Here LSST can play a unique role by accurately characterizing long-period variables (LPVs), a primary distance indicator that can be extended to much greater distances.

- LPVs are hard to characterize because of the long time scales involved (100-1000 days). Major breakthroughs were enabled by the multi-year microlensing surveys of the LMC (MACHO and OGLE) in combination with NIR data from 2MASS, DENIS and the South African/Japanese IRSF. An extension to Local Group spirals (M31, M33) is possible with existing data. LSST would be the first facility that could carry out similar surveys at greater distances and help answer the question of intrinsic variation in the absolute luminosities of the different LPV period-luminosity relations.
- The LSST observations of these nearby ($D < 8$ Mpc) spirals would result in accurate Cepheid distances and the discovery of large LPV populations. This would enable us to accurately calibrate the LPV period-luminosity relations for later application to galaxies that hosted type Ia SNe or even to galaxies in the Hubble flow. This would result in further improvement in the measurement of H_0.

6.4.2 RR Lyrae Stars

While the empirical properties of RR Lyrae stars have been well studied due to their utility as standard candles, theoretical models that help us understand the physics responsible for these properties are not as advanced. For example, it has been known for a long time that Galactic globular clusters divide into two groups (Oosterhoff 1939) based on the mean periods of their ab-type RR Lyrae variables - those that pulsate in the fundamental mode. As shown in Figure 6.6, Oosterhoff Type I clusters have ab-type RR Lyraes with mean periods close to ∼0.56 days while type II clusters, which are more metal-poor, harbor RR Lyraes with mean periods closer to ∼0.66 days (Clement et al. 2001). There have been numerous studies focusing on the Oosterhoff dichotomy trying to understand its origin (e.g. Lee et al. 1990; Sandage 1993). There is evidence to suggest that globular clusters of different Oosterhoff types have different spatial and kinematic properties, perhaps from distinct accretion events in the Galactic halo (Kinman 1959; van den Bergh 1993). There is also evidence favoring the notion that the Oosterhoff Effect is the result of stellar evolution on the horizontal branch (HB). In this scenario, RR Lyraes in type I clusters are evolving from the red HB blueward through the instability strip while those in type II clusters are evolving from the blue HB becoming redward through the instability strip (Lee & Carney 1999). Yet another explanation proposes that the Oosterhoff gap is based on the structure of the envelope in these pulsating stars. Kanbur & Fernando (2005) have suggested that understanding the physics behind the Oosterhoff Effect requires a detailed investigation of the interplay between the photosphere and the hydrogen ionization front in an RR Lyrae variable. Because these features are not co-moving in a pulsating atmosphere, their interaction with each other can affect the period-color relation of RR Lyraes, possibly accounting for the behavior of their mean periods as a function of metallicity and, therefore, helping to explain the Oosterhoff Effect. Clearly the Oosterhoff Effect is one example of a mystery in need of attention from both observers and theoreticians.

One reason there are so many open questions in our theoretical understanding of RR Lyraes and other pulsating variables is that progress requires observations that not only cover the time domain in exquisite detail but also the parameter space of possible pulsation properties in all of their diversity. This is where the LSST will make a significant contribution. We expect to have a substantial number of complete light curves for RR Lyraes in Galactic and Large Magellanic Cloud globular clusters (see the estimate of the RR Lyrae recovery rate in § 8.6.1). In addition, the data set will contain field RR Lyraes in the Milky Way, the LMC, and the SMC, as well as a number of dwarf spheroidal galaxies in the vicinity of the Milky Way. Some of these RR Lyraes may turn out to be members of eclipsing binary systems, further adding to their utility, as described in detail in § 6.10. The depth and breadth of this variability data set will be unprecedented thus facilitating theoretical investigations that have been heretofore impossible.

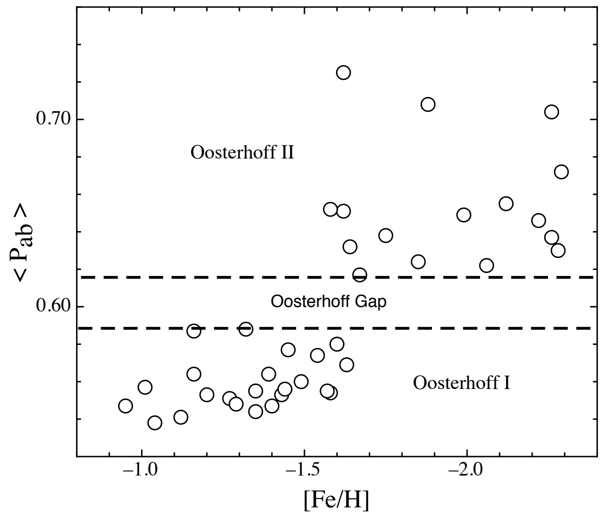

Figure 6.6: Plot of the mean fundamental period for RR Lyraes in Galactic globular clusters, as a function of the cluster metal abundance (from data compiled by Catelan et al. 2005). The two types of Oosterhoff clusters divide naturally on either side of the Oosterhoff gap at 0.6 days.

6.5 A Systematic Survey of Star Clusters in the Southern Hemisphere

Jason Kalirai, Peregrine M. McGehee

6.5.1 Introduction – Open and Globular Star Clusters

Nearby star clusters in the Milky Way are important laboratories for understanding stellar processes. There are two distinct classes of clusters in the Milky Way, population I open clusters, which are lower mass (tens to thousands of stars) and mostly confined to the Galactic disk, and population II globular clusters (tens of thousands to hundreds of thousands of stars), which are very massive and make frequent excursions into the Galactic halo. The systems are co-eval, co-spatial, and iso-metallic, and, therefore, represent controlled testbeds with well-established properties. The knowledge we have gained from studying these clusters grounds basic understanding of how stars evolve, and enables us to interpret light from unresolved galaxies in the Universe.

Despite their importance to stellar astrophysics, most rich star clusters have been relatively poorly surveyed, a testament to the difficulty of observing targets at large distances or with large angular sizes. The advent of wide-field CCD cameras on 4-meter class telescopes has recently provided us with a wealth of new data on these systems. Both the CFHT Open Star Cluster Survey (Kalirai et al. 2001a, see Figure 6.7) and the WIYN Open Star Cluster Survey (Mathieu 2000) have systematically imaged nearby northern hemisphere clusters in multiple filters, making possible new global studies. For example, these surveys have refined our understanding of the fundamental properties (e.g., distance, age, metallicity, reddening, binary fraction, and mass) of a large set of clusters and begun to shed light on the detailed evolution of stars in post main sequence phases (e.g., total integrated stellar mass loss) right down to the white dwarf cooling sequences (Kalirai et al. 2008).

Even the CFHT and WIYN Open Star Cluster Surveys represent pencil beam studies in comparison to LSST. The main LSST survey will provide homogeneous photometry of stars in all nearby star clusters in the southern hemisphere (where no survey of star clusters has ever been undertaken). The LSST footprint contains 419 currently known clusters; of these, 179 are within 1 kpc, and several are key benchmark clusters for testing stellar evolution models. Only 15 of the clusters in the LSST footprint, however, have more than 100 known members in the WEBDA database, demonstrating the relative paucity of information known about these objects. LSST's deep, homogeneous, wide-field photometry will greatly expand this census, discovering new, previously unknown clusters and providing a more complete characterization of the properties and membership of clusters already known to exist. Analysis of this homogeneous, complete cluster sample will enable groundbreaking advances in several fields, which we describe below.

6.5.2 New Insights on Stellar Evolution Theory

A century ago, Ejnar Hertzsprung and Henry Norris Russell found that stars of the same temperature and the same parallax and, therefore, at the same distance, could have very different luminosities (Hertzsprung 1905; Russell 1913, 1914). They coined the terms "giants" and "dwarfs" to describe these stars, and the initial work quickly evolved into the first Hertzsprung-Russell (H-R) Diagram in 1911.

The H-R diagram has since become one of the most widely used plots in astrophysics, and understanding stellar evolution has been one of the most important pursuits of observational astronomy. Much of our knowledge in this field, and on the ages of stars, is based on our ability to understand and model observables in this plane, often for nearby stellar populations. This knowledge represents fundamental input into our understanding of many important astrophysical processes. For example, stellar evolution aids in our understanding of the formation of the Milky Way (e.g., through age dating old stellar populations, Krauss & Chaboyer 2003), the history of star formation in other galaxies (e.g., by interpreting the light from these systems with population synthesis models), and chemical evolution and feedback processes in galaxies (e.g., by measuring the rate and timing of mass loss in evolved stars).

With the construction of sensitive wide-field imagers on 4-m and 8-m telescopes, as well as the launch of the HST, astronomers have recently been able to probe the H-R diagram to unprecedented depths and accuracy for the nearest systems (e.g., Richer et al. 2008). These studies have

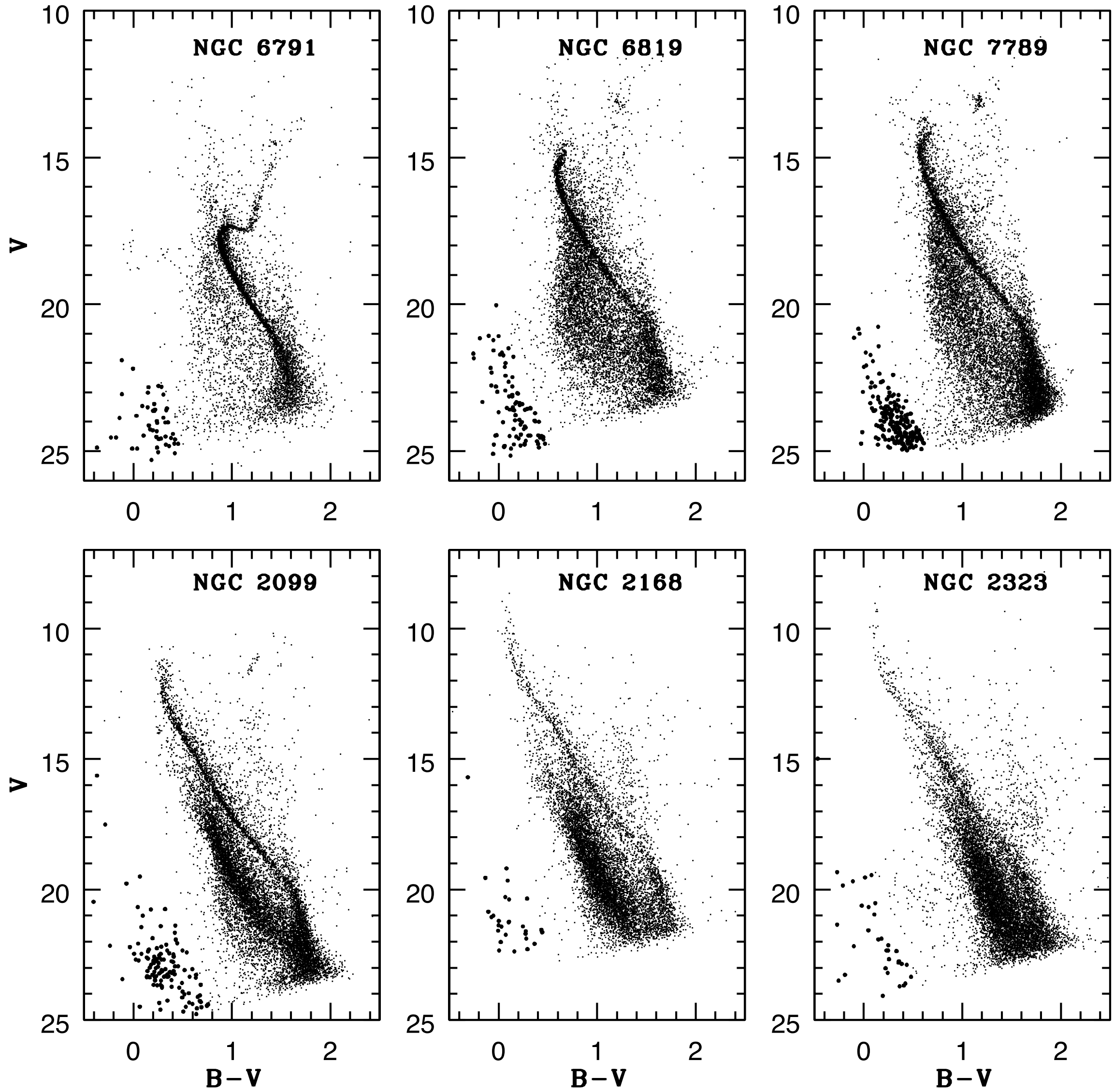

Figure 6.7: Color-magnitude diagrams of six rich open star clusters observed as a part of the Canada-France-Hawaii Telescope Open Star Cluster Survey (Kalirai et al. 2001a). The clusters are arranged from oldest in the top-left corner (8 Gyr) to the youngest in the bottom-right corner (100 Myr). Each color-magnitude diagram presents a rich, long main sequence stretching from low mass stars with $M \lesssim 0.5\ M_{\odot}$ up through the turn-off, including post-main sequence evolutionary phases. The faint blue parts of each color-magnitude diagram illustrate a rich white dwarf cooling sequence (candidates shown with larger points).

made possible detailed comparisons of not only the positions of stars in the H-R diagram with respect to the predictions of theoretical models, but also a measurement of the distribution of stars along various evolutionary phases (e.g., Kalirai & Tosi 2004). Such comparisons provide for a more accurate measurement of the properties of each system (e.g., the age), and also yield important insight into the binary fraction, initial mass function, and initial mass of the clusters. Unfortunately, these comparisons have thus far been limited to those clusters that are nearby and for which we have such photometry, thus only sampling a small fraction of age/metallicity space.

LSST will yield homogeneous photometry of star clusters in multiple bands down to well below the main sequence turn-off, out to unprecedented distances, and, therefore, will provide a wealth of observational data to test stellar evolution models. With a detection limit of 24 – 25th magnitude in the optical bandpasses in a single visit, and a co-added 5-σ depth in the r-band of 27.8, LSST will yield accurate turn-off photometry of all star clusters in its survey volume out to beyond the edge of the Galaxy. For a 12 Gyr globular cluster, this photometry will extend over three magnitudes below the main sequence turn-off.

The H-R diagrams LSST will produce for thousands of star clusters will completely fill the metallicity/age distribution from [Fe/H] $= -2$, 12 Gyr globular clusters to super-solar open clusters with ages of a few tens of millions of years (including those in the LMC and SMC). The multi-band photometry will constrain the reddenings to each cluster independently and, therefore, allow for detailed tests of the physics involved in the construction of common sets of models, as well as atmospheric effects. For example, slope changes and kinks along the main sequence can yield valuable insights into the treatment of convection and core-overshooting, the importance of atomic diffusion and gravitational settling (Vandenberg et al. 1996; Chaboyer 2000), and the onset of rotational mixing in massive stars (e.g., younger clusters). Examples of these effects on the color-magnitude diagrams can be seen in Figure 6.7, for example, from the morphology of the hook at the main sequence turn-off in NGC 6819, NGC 7789, and NGC 2099, and the slope of the main sequence in NGC 2099 at $V = 14 - 16$. For the first time, these comparisons can be carried out in sets of clusters with different ages but similar metallicity, or vice versa, thus fixing a key input of the models. Taken further, the data may allow for new probes into the uncertainties in opacities, nuclear reaction rates, and the equation of state, and, therefore, lead to new understandings on both the micro- and macrophysics that guide stellar evolution theory.

6.5.3 The Stellar Mass Function

An important goal of stellar astrophysics in our local neighborhood is to characterize the properties of low luminosity stars on the lower main sequence; such studies will be greatly advanced by the LSST data, as described in more detail in § 7.4. Such studies feed into our knowledge of the color-magnitude relation and the initial mass function of stars, which themselves relate to the physics governing the internal and atmospheric structure of stars. In fact, knowledge of possible variations in the initial mass function has widespread consequences for many Galactic and extragalactic applications (e.g., measuring the star formation mechanisms and mass of distant galaxies). Measuring these distributions in nearby star clusters, as opposed to the field, offers key advantages as the stars are all at the same distance and of the same nature (e.g., age and metallicity).

Previous surveys such as the SDSS and 2MASS have yielded accurate photometry of faint M dwarfs out to distances of ∼2 kpc. LSST, with a depth that is two and five magnitudes deeper than Pan-STARRS and Gaia respectively, will enable the first detection of such stars to beyond 10 kpc. At this distance, the color-magnitude relation of hundreds of star clusters will be established and permit the first systematic investigation of variations in the relation with age and metallicity. The present day mass functions of the youngest clusters will be dynamically unevolved and, therefore, provide for new tests of the variation in the initial mass function as a function of environment. Even for the older clusters, the present day mass function can be related back to the initial mass function through dynamical simulations (e.g., Hurley et al. 2008), enabling a comparison between these cluster mass functions and that derived from LSST detections of Milky Way field stars.

6.5.4 A Complete Mass Function of Stars: Linking White Dwarfs to Main Sequence Stars

The bulk of the mass in old stellar populations is now tied up in the faint remnant stars of more massive evolved progenitors. In star clusters, these white dwarfs can be uniquely mapped to their progenitors to probe the properties of the now evolved stars (see § 6.11 below). The tip of the sequence, formed from the brightest white dwarfs, is located at $M_V \sim 11$ and will be detected by LSST in thousands of clusters out to 20 kpc. For a 1 Gyr (10 Gyr) cluster, the faintest white dwarfs have cooled to $M_V = 13$ (17), and will be detected in clusters out to 8 kpc (1 kpc). These white dwarf cooling sequences not only provide direct age measurements (e.g., Hansen et al. 2007) for the clusters and, therefore, fix the primary leverage in theoretical isochrone fitting, allowing secondary effects to be measured, but also can be followed up with current Keck, Gemini, Subaru, and future (e.g., TMT and/or GMT) multi-object spectroscopic instruments to yield the mass distribution along the cooling sequence. These mass measurements represent the critical input to yield an initial-final mass relation (Kalirai et al. 2008) and, therefore, provide the progenitor mass function above the present day turn-off. The relations, as a function of metallicity, will also yield valuable insight into mass loss mechanisms in post-main sequence evolution and test for mass loss-metallicity correlations. The detection of these white dwarfs can, therefore, constrain difficult-to-model phases such as the asymtotic giant branch (AGB) and planetary nebula (PN) stages.

6.5.5 The Utility of Proper Motions

The temporal coverage of LSST will permit the science discussed above to be completed on a proper motion cleaned data set. To date, only a few star clusters have such data down to the limits that LSST will explore. Those large HST data sets of specific, nearby systems that we do currently possess (e.g., Richer et al. 2008) demonstrate the power of proper motion cleaning to produce exquisitely clean H-R diagrams. Tying the relative motions of these cluster members to an extragalactic reference frame provides a means to measure the space velocities of these systems and, therefore, constrain their orbits in the Galaxy. As open and globular clusters are largely confined to two different components of the Milky Way, these observations will enable each of these types of clusters to serve as a dynamical tracer of the potential of the Milky Way and help us understand the formation processes of the disk and halo (e.g., combining the three-dimensional distance, metallicity, age, and star cluster orbit).

6.5.6 Transient Events and Variability in the H-R Diagram

The finer cadence of LSST's observations will also yield the first homogeneous survey of transient and variable events in a well studied sample of clusters (cataclysmic variables, chromospherically active stars, dwarf novae, etc.). For each of these systems, knowledge of their cluster environment yields important insight into the progenitors of the transients, information that is typically missing for field stars. Virtually all of the Galactic transient and variable studies outlined in this chapter and in Chapter 8 will be possible within these star clusters.

6.6 Decoding the Star Formation History of the Milky Way

Kevin R. Covey, Phillip A. Cargile, Saurav Dhital

Star formation histories (SFHs) are powerful tools for understanding galaxy formation. Theoretical simulations show that galaxy mergers and interactions produce sub–structures of stars sharing a single age and coherent spatial, kinematic, and chemical properties (Helmi & White 1999; Loebman et al. 2008). The nature of these sub–structures places strong constraints on models of structure formation in a ΛCDM universe (Freeman & Bland-Hawthorn 2002).

The Milky Way is a unique laboratory for studying these Galactic sub-structures. Detailed catalogs of stars in the Milky Way provide access to low contrast substructures that cannot be detected in more distant galaxies. Photometric and spectroscopic surveys have identified numerous spatial–kinematic–chemical substructures: the Sagittarius dwarf, Palomar 5's tidal tails, the Monoceros Ring, etc. (Ibata et al. 1994; Odenkirchen et al. 2001; Yanny et al. 2003; Grillmair 2006; Belokurov et al. 2006). LSST and ESO's upcoming Gaia mission will produce an order of magnitude increase in our ability to identify such spatial–kinematic substructures (see Sections 7.1, 7.2, and 6.12).

Our ability to probe the Galactic star formation history has severely lagged these rapid advances in the identification of spatial–kinematic–chemical sub–structures. Age distributions have been constructed for halo globular clusters and open clusters in the Galactic disk (de la Fuente Marcos & de la Fuente Marcos 2004), but the vast majority of clusters dissipate soon after their formation (Lada & Lada 2003), so those that persist for more than 1 Gyr are a biased sub–sample of even the clustered component of the Galaxy's star formation history. The star formation histories of distributed populations are even more difficult to derive: in a seminal work, Twarog (1980) used theoretical isochrones and an age–metallicity relation to estimate ages for Southern F dwarfs and infer the star formation history of the Galactic disk. The star formation history of the Galactic disk has since been inferred from measurements of several secondary stellar age indicators: chromospheric activity–age relations (Barry 1988; Soderblom et al. 1991; Rocha-Pinto et al. 2000; Gizis et al. 2002; Fuchs et al. 2009); isochronal ages (Vergely et al. 2002; Cignoni et al. 2006; Reid et al. 2007); and white dwarf luminosity functions (Oswalt et al. 1996; Harris et al. 2006). Despite these significant efforts, no clear consensus has emerged as to the star formaiton history of the thin disk of the Galaxy: most derivations contain episodes of elevated or depressed star formation, but these episodes rarely coincide from one study to the next, and their statistical significance is typically marginal ($\sim 2\sigma$).

Two questions at the next frontier in stellar and Galactic archeology are: How well can we understand and calibrate stellar age indicators? What is the star formation history of the Milky Way, and what does it tell us about galaxy formation and evolution? Answering these questions requires LSST's wide-field, high-precision photometry and astrometry to measure proper motions, parallaxes, and time–variable age indicators (rotation, flares, and so on) inaccessible to Gaia. Aspects of LSST's promise in this area are described elsewhere this science book; see, for example, the discussions of LSST's promise for measuring the age distribution of Southern Galactic Star Clusters (§ 6.5), identifying the lowest metallicity stars (§ 6.7), and deriving stellar ages from white dwarf cooling curves (§ 6.11). Here, we describe three techniques (gyrochronology, age–activity relations, and binary star isochronal ages) that will allow LSST to provide reliable ages for individual field stars, unlocking fundamentally new approaches for understanding the SFH of the Milky Way.

6.6.1 Stellar Ages via Gyrochronology

Since the seminal observations by Skumanich (1972), we have known that rotation, age, and magnetic field strength are tightly coupled for solar–type stars. This relationship reflects a feedback loop related to the solar–type dynamo's sensitivity to inner rotational shear: fast rotators generate strong magnetic fields, launching stellar winds that carry away angular momentum, reducing the star's interior rotational shear and weakening the star's magnetic field. This strongly self–regulating process ultimately drives stars with the same age and mass toward a common rotation period.

Over the past decade, the mass–dependent relationship between stellar rotation and age has been calibrated for the first time (Barnes 2003; Meibom et al. 2008; Mamajek & Hillenbrand 2008). These calibrations are based on rotation periods measured for members of young clusters ($t < 700$ Myrs) and the Sun, our singular example of an old ($t \sim 4.5$ Gyrs), solar–type star with a precise age estimate. The Kepler satellite is now acquiring exquisite photometry for solar–type stars in NGC 6819 and NGC 6791, providing rotation periods for stars with ages of 2.5 and 8 Gyrs, respectively, and placing these gyrochronology relations on a firm footing for ages greater than 1 Gyr (Meibom 2008).

We have performed a detailed simulation to identify the domain in age–distance–stellar mass space where LSST will reliably measure stellar rotation periods, and thus apply gyrochronology relations to derive ages for individual field stars. We begin with a detailed model of a rotating, spotted star, kindly provided by Frasca et al. (private communication). Adopting appropriate synthetic spectra for the spotted and unspotted photosphere, the disk-averaged spectrum is calculated as a function of stellar rotational phase; convolving the emergent flux with the LSST bandpasses produces synthetic light curves for rotating spotted stars (see Figure 6.8). Using this model, we produced a grid of synthetic r band light curves for G2, K2, and M2 dwarf stars with ages of 0.25, 0.5, 1.0, 2.5, and 5.0 Gyrs. The rotation period and spot size were set for each model to reproduce the age-period-amplitude relations defined by Mamajek & Hillenbrand (2008) and Hartman et al. (2009). An official LSST tool (`Interpolator0.9`, S. Krughoff, private communication) then sampled this grid of synthetic light curves with the cadence and observational uncertainties appropriate for the main LSST survey.

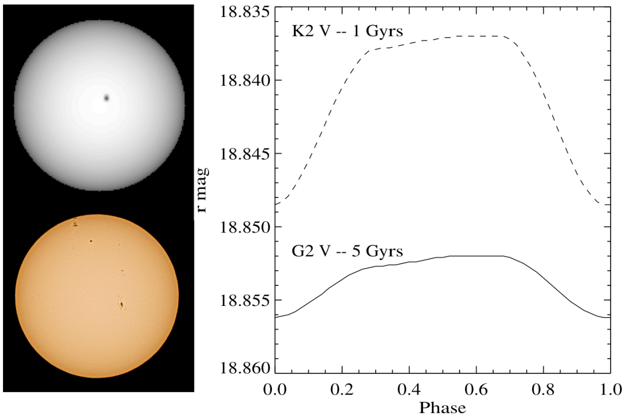

Figure 6.8: *Left:* Comparison of our synthetic model of a 5 Gyr solar analog (top panel; image produced by A. Frasca's star spot light curve modeling code, Macula.pro) with an actual image of the Sun (bottom panel) from Loyd Overcash, with permission. *Right:* Synthetic LSST light curves for the 5 Gyr Solar analog model shown above (solid line), as well as for a 1 Gyr K2 dwarf.

We identify rotation periods from these simulated LSST light curves using a Lomb-Scargle periodogram (Scargle 1982; Horne & Baliunas 1986), where we identify the most significant frequency in the Fourier transform of the simulated light curve. Folding the data at the most significant frequency then allows visual confirmation of the rotation period. Figure 6.9 shows the unfolded light curve, the periodogram, and the folded light curve for a K2 star of age 2.5 Gyr "observed" at $r = 19$ and 21. As the first panel of each row shows, the noise starts to swamp the signal at fainter magnitudes, making it harder to measure the period. This problem is most important for the oldest stars: with diminished stellar activity producing small starspots, these stars have light curves with small amplitudes. However, with LSST's accuracy, we will still be able to measure periods efficiently for G, K, and early-M dwarfs with $r \leq 20$ and ages $\lesssim$2 Gyr. All periods in these regimes were recovered, without prior knowledge of the rotation period. At older ages and fainter magnitudes, the periodogram still finds peaks at the expected values, but the power is low and the folded light curves are not convincing. Periods could potentially be recovered from lower amplitude and/or noisier light curves by searching for common periods across LSST's multiple bandpasses; with coverage in the $ugrizy$ bands, at least four of the bands are expected to exhibit the periodicity. This will allow us to confirm rotation periods using light curves with low amplitudes in a single band by combining the results at the various bands.

Our simulations indicate LSST will be able to measure rotation periods of 250 Myr solar analogs between 1 and 20 kpc; the inner distance limit is imposed by LSST's $r \sim 16$ saturation limit, and the outer distance limit identifies where LSST's photometric errors are sufficiently large to prevent detection of photometric variations at the expected level. Older solar analogs will have smaller photometric variations, reducing the distance to which periods can be measured: LSST will measure periods for 5 Gyr solar analogs over a distance range from 1 to 8 kpc. Lower mass M dwarfs, which are significantly fainter but also much more numerous, will have reliable rotation period measurements out to 500 pc for stars as old as 5 Gyrs. Measuring photometric rotation periods for thousands of field stars in a variety of Galactic environments, LSST will enable gyrochronology relations to map out the SFH of the Galactic disk over the past 1-2.5 Gyrs, and as far back as 5 Gyrs for brighter stars within the extended solar neighborhood.

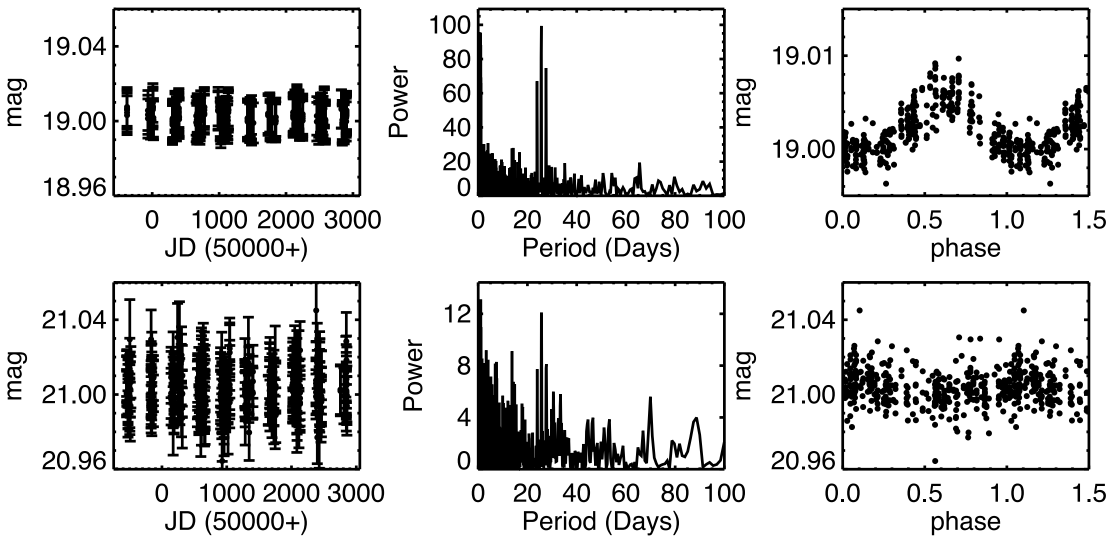

Figure 6.9: The unfolded light curve, Lomb-Scargle periodogram, and the folded light curve for a K2 dwarf of age 2.5 Gyr with $r = 19$ and 21 magnitudes. We were able to easily recover the period at the bright end, with the efficiency decreasing at the faint end, especially for older stars, as noise starts to dominate. Our search through parameter space shows that rotation periods can be recovered for G to early–M spectral types, for ages up to a few Gyrs, and up to $r = 21$ (see text for a detailed description).

LSST will also significantly improve our understanding of the gyrochronology relations that form the foundation of this analysis. One fundamental requirement of any stellar dating technique, including gyrochronology, is that it should be able to accurately predict the age of an object (or collection of objects) whose age(s) we know very well from an independent measure. Open clusters (§ 6.5) with precise age determinations are essential to this calibration process.

The LSST footprint contains several open clusters that are critical testbeds for testing of stellar evolution theory over the first 0.5 Gyrs (see Table 6.1). These clusters have precise age estimates from robust dating techniques (e.g., lithium depletion boundary ages) and, therefore, will provide the necessary calibration to accurately determine how stellar rotation evolves with age over the initial portion of each star's lifetime.

Table 6.1: Young LSST Benchmark Open Clusters

Cluster	Age [Myr]	Distance [pcs]	[Fe/H]	Known Members	Spectral Type at LSST Limit	M_z limit
ONC (NGC 1976)	1	414	0.00	733	L3	15.92
NGC 2547	35	474	-0.16	69	L1	15.65
IC 2602/IC 2391	50	145/149	-0.09	196/94	T5	17.93
Blanco 1	80	207	0.04	128	L6	16.84
NGC 2516	120	344	0.06	130	L2	15.79
NGC 3532	355	411	-0.02	357	L1	15.51

Table 6.2: Selection of Old LSST Open Clusters

Cluster	Age [Myr]	Distance [pcs]	[Fe/H]	Known Members	Spectral Type at LSST Limit	M_z limit
IC 4651	1140	888	0.09	16	L0	14.08
Ruprecht 99	1949	660	...	7	L1	14.83
NGC 1252	3019	640	...	22	L2	14.94
NGC 2243	4497	4458	-0.44	8	M5	10.68
Berkeley 39	7943	4780	-0.17	12	M5	10.43
Collinder 261	8912	2190	-0.14	43	M6	11.90

In addition, the WEBDA open cluster database lists over 400 known open clusters in the LSST footprint; many of these have poorly constrained cluster memberships (e.g., fewer than 20 known members), especially for the oldest clusters (for example, see Table 6.2). LSST's deep, homogeneous photometry and proper motions will significantly improve the census of each of these cluster's membership, providing new test cases for gyrochronology in age domains not yet investigated with this dating technique.

6.6.2 Stellar Ages via Age–Activity Relations

Age–activity relations tap the same physics underlying the gyrochronology relations (West et al. 2008; Mamajek & Hillenbrand 2008), and provide an opportunity to sample the star formation history of the Galactic disk at ages inaccessible to gyrochronology. Although inherently intermittent and aperiodic, stellar flares, which trace the strength of the star's magnetic field, are one photometric proxy for stellar age that will be accessible to LSST. The same cluster observations that calibrate gyrochronology relations will indicate how the frequency and intensity of stellar flares vary with stellar age and mass (see § 8.9.1), allowing the star formation history of the Galactic disk to be inferred from flares detected by LSST in field dwarfs. The primary limit on the lookback time of a star formation history derived from stellar flare rates relations is the timescale when flares become too rare or weak to serve as a useful proxy for stellar age. We do not yet have a calibration of what this lifetime is, but early explorations suggest even the latest M dwarfs become inactive after ∼5 Gyrs (Hawley et al. 2000; West et al. 2008).

6.6.3 Isochronal Ages for Eclipsing Binaries in the Milky Way Halo

Halo objects are ∼0.5% of the stars in the local solar neighborhood, so the ages of nearby high velocity stars provide a first glimpse of the halo's star formation history. The highly substructured nature of the Galactic halo, however, argues strongly for sampling its star formation history in situ to understand the early Milky Way's full accretion history. The stellar age indicators described in the previous sections are not useful for probing the distant halo, as stellar activity indicators (rotation, flares) will be undetectable for typical halo ages.

Eclipsing binary stars (EBs; § 6.10), however, provide a new opportunity for measuring the SFH of the distributed halo population. Combined analysis of multi-band light curves and radial velocity measurements of detached, double–lined EBs yield direct and accurate measures of the masses, radii, surface gravities, temperatures, and luminosities of the two stars (Wilson & Devinney 1971; Prša & Zwitter 2005). This wealth of information enables the derivation of *distance independent* isochronal ages for EBs by comparing to stellar evolution models in different parameter spaces, such as the mass–radius plane. Binary components with $M > 1.2M_{\odot}$ typically appear co–eval to within 5%, suggesting that the age estimates of the individual components are reliable at that level (Stassun et al. 2009). Lower mass binary components have larger errors, likely due to the suppression of convection by strong magnetic fields (López-Morales 2007); efforts to include these effects in theoretical models are ongoing, and should allow for accurate ages to be derived for lower–mass binaries as well. By identifying a large sample of EBs in the Milky Way halo, LSST will enable us to begin mapping out the star formation history of the distributed halo population.

6.7 Discovery and Analysis of the Most Metal Poor Stars in the Galaxy

Timothy C. Beers

Metal-poor stars are of fundamental importance to modern astronomy and astrophysics for a variety of reasons. This long and expanding list includes:

- **The Nature of the Big Bang:** Standard Big Bang cosmologies predict, with increasing precision, the amount of the light element lithium that was present in the Universe after the first minutes of creation. The measured abundance of Li in very metal-poor stars is thought to provide a direct estimate of the single parameter in these models, the baryon-to-photon ratio.
- **The Nature of the First Stars:** Contemporary models and observational constraints suggest that star formation began no more than a few hundred million years after the Big Bang, and was likely to have been responsible for the production of the first elements heavier than Li. The site of this first element production has been argued to be associated with the explosions of stars with characteristic masses up to several hundred solar masses. These short-lived objects may have provided the first "seeds" of the heavy elements, thereby strongly influencing the formation of subsequent generations of stars.
- **The First Mass Function:** The distribution of masses with which stars have formed throughout the history of the Universe is of fundamental importance to the evolution of galaxies. Although the Inital Mass Function (IMF) today appears to be described well by simple power laws, it is almost certainly different from the First Mass Function (FMF), associated with the earliest star formation in the Universe. Detailed studies of elemental abundance patterns in low-metallicity stars provide one of the few means by which astronomers might peer back and obtain knowledge of the FMF.
- **Predictions of Element Production by Supernovae:** Modern computers enable increasingly sophisticated models for the production of light and heavy elements by supernovae

explosions. Direct insight into the relevant physics of these models can be obtained from inspection of the abundances of elements in the most metal-deficient stars, which presumably have not suffered pollution from numerous previous generations of stars.

- **The Nature of the Metallicity Distribution Function (MDF) of the Galactic Halo:** Large samples of metal-poor stars are now making it possible to confront detailed Galactic chemical evolution models with the observed distributions of stellar metallicities. Tests for structure in the MDF at low metallicity, the constancy of the MDF as a function of distance throughout the Galactic halo, and the important question of whether we are approaching, or have already reached, the limit of low metallicity in the Galaxy can all be addressed with sufficiently large samples of very metal-poor stars.
- **The Astrophysical Site(s) of Neutron-Capture Element Production:** Elements beyond the iron peak are formed primarily by captures of neutrons, in a variety of astrophysical sites. The two principal mechanisms are referred to as the slow (s)-process, in which the time scales for neutron capture by iron-peak seeds are longer than the time required for beta decay, and the rapid (r)-process, where the associated neutron capture occurs faster than beta decay. These are best explored at low metallicity, where one is examining the production of heavy elements from a limited number of sites, perhaps even a single site.

Owing to their rarity, the road to obtaining elemental abundances for metal-poor stars in the Galaxy is long and arduous. The process usually involves three major observational steps: 1) A wide-angle survey must be carried out, and candidate metal-poor stars selected; 2) Moderate-resolution spectroscopic follow-up of candidates is required to validate the genuine metal-poor stars among them; and finally, 3) High-resolution spectroscopy of the most interesting candidates emerging from step 2) must be obtained.

The accurate *ugriz* photometry obtained by LSST will provide for the photometric selection of metal-poor candidates from the local neighborhood out to over 100 kpc from the Galactic center. Similar techniques have been (and are being) employed during the course of SDSS-II and SDSS-III in order to identify candidate very metal-poor ([Fe/H] < -2.0) stars for subsequent follow-up with medium-resolution ($R = 2000$) spectroscopic study with the SDSS spectrographs. This approach has been quite successful, as indicated by the statistics shown in § 6.7, based on work reported by Beers et al. (2009). See Beers & Christlieb (2005) for more discussion of the classes of metal-poor stars.

Table 6.3: Impact of SDSS on Numbers of Metal-Poor Stars

[Fe/H]	Pre SDSS-II	Post SDSS-II
< -1.0	~ 15000	150000+
< -2.0	~ 3000	30000+
< -3.0	~ 400	1000+
< -4.0	5	5
< -5.0	2	2
< -6.0	0	0

LSST photometric measurements will be more accurate than those SDSS obtains (Ivezić et al.

2008a) (Table 1.1). This has three immediate consequences: 1) Candidate metal-poor stars will be far more confidently identified, translating to much more efficient spectroscopic follow-up; 2) Accurate photometric metallicity estimates will be practical to obtain down to substantially lower metallicity (perhaps [Fe/H] < -2.5) than is feasible for SDSS photometric selection ([Fe/H] $\simeq -2.0$); and 3) The much deeper LSST photometry means that low-metallicity stars will be identifiable to 100 kpc, covering a thousand times the volume that SDSS surveyed. The photometrically determined metallicities from LSST will be of great scientific interest, as they will enable studies of the changes in stellar populations as a function of distance based on a sample that includes over 99% of main sequence stars in the LSST footprint. This sample will also enable studies of the correlations between metallicity and stellar kinematics based on measured proper motions (for an SDSS-based example, see Ivezić et al. 2008a). Detailed metallicity measurements will of course require high S/N, high-resolution spectroscopic follow-up of the best candidates.

Proper motions obtained by LSST will also enable spectroscopic targeting of what are likely to be some of the most metal-poor stars known, those belonging to the so-called outer-halo population. Carollo et al. (2007) used a sample of some 10,000 "calibration stars" with available SDSS spectroscopy, and located within 4 kpc of the Sun, to argue that the halo of the Galaxy comprises (at least) two distinct populations: a slightly prograde inner halo (which dominates within 10 kpc) with an MDF that peaks around [Fe/H] $= -1.6$ and an outer halo (which dominates beyond 15-20 kpc) in net retrograde rotation with an MDF that peaks around [Fe/H] $= -2.2$. The expectation is that the tail of the outer-halo MDF will be populated by stars of the lowest metallicities known. Indeed, all three stars recognized at present with [Fe/H] < -4.5, including two stars with [Fe/H] < -5.0, exhibit characteristics of membership in the outer-halo population. Stars can be selected from LSST with proper motions that increase their likelihood of being members of this population either based on large motions consistent with the high-energy outer-halo kinematics, or with proper motion components suggesting highly retrograde orbits.

6.8 Cool Subdwarfs and the Local Galactic Halo Population

Sébastien Lépine, Pat Boeshaar, Adam J. Burgasser

Cool subdwarfs are main sequence stars, which have both a low mass and a low abundance of metals. Locally they form the low-mass end of the stellar Population II. Cool subdwarfs have historically been identified from catalogs of stars with large proper motion, where they show up as high velocity stars. Kinematically they are associated with the local thick disk and halo populations. Because they are the surviving members of the earliest generations of stars in the Galaxy with evolutionary timescales well exceeding a Hubble time, cool subdwarfs are true fossils of the early history of star formation in the Galaxy, and hold important clues to the formation of the Galactic system. While these stars have already traveled dozens of orbits around the Galaxy and undergone some dynamical mixing, a study of their orbital characteristics and metallicity distribution can still shed light on the formation and dynamical evolution of our Galaxy. In particular, cool subdwarfs do not undergo any significant enrichment of their atmospheres, but largely retain their original elemental composition from the time of their birth. This makes them perfect tracers of the early chemical composition of the gas that formed these first generations of low-mass stars.

Cool stars of spectral type M have atmospheres that are dominated by molecular bands from metal hydrides and oxides, most notably CaH, FeH, TiO, and VO. Metallicity variations result in marked differences in the absolute and relative strengths of these bands. As a result, M dwarfs and subdwarfs also display significant variations in their broadband colors depending on their metal abundances. The significantly metal-poor subdwarfs from the Galactic halo populate a distinct locus in the $g - r/r - i$ color-color diagram. The strong color-dependence makes the M subdwarfs easy to identify (Figure 6.10), and also potentially allows one to determine the metallicity from broadband photometry alone. The only caveat is that this part of color-color space is also populated by extragalactic sources, which may be distinguishable by their extent and their zero proper motions.

In Figure 6.11 panels, the blue line shows the mean positions of Pickles (1998) main sequence stars, the dots refer to quasars from $z = 0$ to 5, and the mean position of the coolest ultra-, extreme-, and M subdwarfs are noted by crosses in *grizy* color space. Redshifting the locally observed elliptical galaxy template (Coleman et al. 1980) over the range $z = 0 - 2$ clearly results in colors that occupy the same color space as the subdwarfs of all classes, and even extend into the region of the coolest subdwarfs. Estimates from the Deep Lens Survey (Boeshaar et al. 2003) indicate that at high Galactic latitudes, up to 30% of the "stellar" objects with M subdwarf colors detected at 23-25 mag in $\geq 1''$ seeing will actually be unresolved ellipticals at $z = 0.25 - 1$. The $g - z$ vs. $z - y$ plot clearly separates the high redshift quasars from the subdwarf region, but quasars should be only a minor contaminant due to their low spatial density. The net effect of including evolution into stellar population models is to shift the elliptical tracks by several tenths of a magnitude in $g - r$ and $r - i$. Thus unresolved ellipticals may still fall within the overlap envelope. Additional synthetic $z - y$ colors for stars, brown dwarfs plus quasars and unevolved galaxies as a function of redshift with color equations between the UKIRT Wide-Field Camera and SDSS can be found in Hewett et al. (2006). A proper motion detection is thus required for formal identification.

Very large uncertainties in the luminosity function and number density of such objects exist (Digby et al. 2003). It is not known whether the subdwarfs have a mass function similar to that of the disk stars. Their metallicity distribution is also poorly constrained. The main limitation in using the low-mass subdwarfs to study the Galactic halo resides in their relatively low luminosities. M subdwarfs have absolute magnitudes in the range $10 < M_r < 15$. With the SDSS magnitude limit of $r = 22$ and proper motion data to only $r = 20$, M subdwarfs can thus only be detected out to a few hundred parsecs. With a local density yielding $\sim 1{,}000$ objects within 100 parsecs of the Sun (all-sky), SDSS can only formally identify a few thousand M subdwarfs.

LSST will open the way for a study of the low-mass halo stars on a much grander scale. With photometry to $r \simeq 27$ and proper motion data available to $r = 24.5$, the LSST survey will detect all stellar subdwarfs to 1 kiloparsec. In the Sun's vicinity, halo stars have large transverse velocities ($v_T > 100$ km s^{-1}), which yield proper motions $\mu > 20$ mas yr^{-1} up to 1 kpc. With the required proper motion accuracy of 0.2 mas yr^{-1} for LSST, virtually all the subdwarfs will be confirmed through proper motion detection. The ability to estimate metallicity classes for the halo subdwarfs based on the LSST *gri* magnitudes alone will make it possible to determine the approximate metallicity distribution of the halo stars from an unprecedented sample of >500,000 objects.

Relatively accurate photometric distances can also be determined for low-mass stars, yielding distances generally accurate to better than 50%. These, combined with the proper motion data,

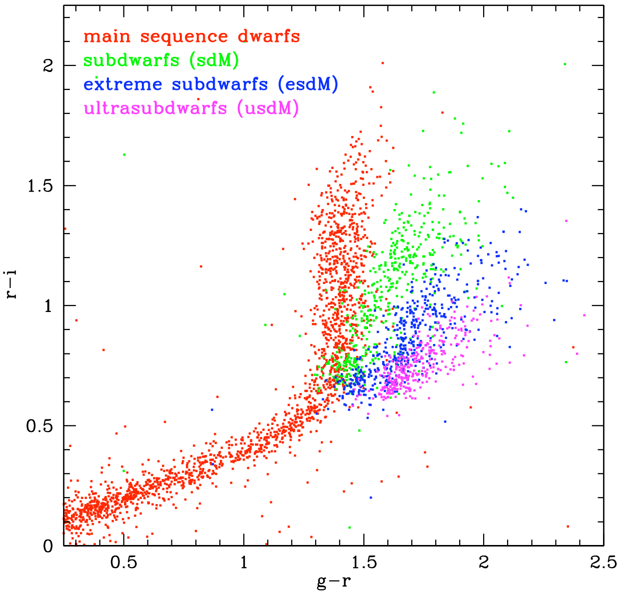

Figure 6.10: Distribution of cool subdwarfs in the $g-r/r-i$ color-color diagram. The four metallicity classes (dwarfs, subdwarfs, extreme subdwarfs, and ultrasubdwarfs) are represented in different colors. The segregation according to metallicity class allows one to identify the halo subdwarfs and estimate their metallicities (and temperatures) based on photometry alone. Photometric data and spectroscopic confirmation of the stars have been obtained from SDSS.

will make it possible to plot large numbers of stars in tangential velocity space and search for possible substructure in the tangential velocity space distribution.

Besides determining the subdwarf number density and distribution in metallicity, mass, and luminosity, the exploration of the time domain by LSST will identify eclipsing doubles, monitor rotational modulation, and search for unexpected flaring activity. The multiplicity fraction of the halo population is only weakly constrained due to the paucity of subdwarfs and their greater distances relative to their main sequence counterparts. A direct comparison with the number of eclipsing binaries also expected to be discovered among the disk stars will determine whether close double stars are more or less common in the halo population. More critically, no eclipsing system comprised of cool subdwarfs has ever been identified, but LSST's systematic monitoring has excellent prospects for finding at least several sdM+sdM eclipsing systems. Such systems would be immensely useful in determining the mass and radii of low-mass, metal-poor stars, which is now poorly constrained due to a paucity of known binary systems.

Beyond building up very large samples of M-type subdwarfs, LSST will also uncover the first substantial samples of cooler L-type subdwarfs, metal-deficient analogs to the L dwarf population of very low mass stars and brown dwarfs (Burgasser et al. 2008). L subdwarfs have masses spanning the metallicity-dependent, hydrogen-burning limit, making them critical probes of both low-mass star formation processes in the halo and thermal transport in partially degenerate stellar interiors. The subsolar metallicities of L subdwarfs are also important for testing chemistry models of low-temperature stellar and brown dwarf photospheres, in particular condensate grain and cloud formation, a process that largely defines the properties of L dwarfs but may be inhibited or absent in L subdwarfs (Burgasser et al. 2003a; Reiners & Basri 2006). Only a few L subdwarfs have been

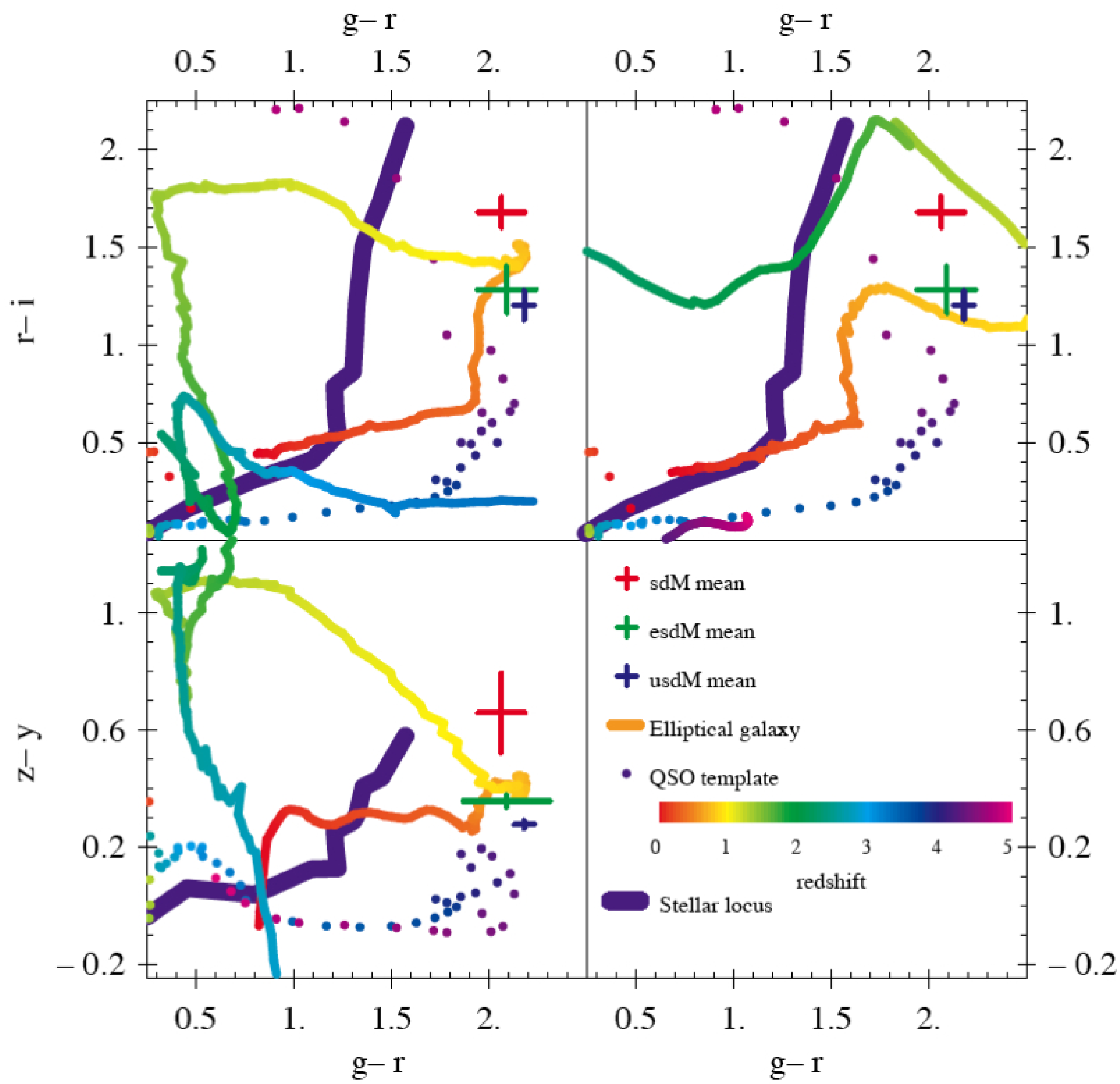

Figure 6.11: *Upper left:* $g - r/r - i$ color-color diagram similar to Figure 6.10 showing the location of the main sequence stars (purple line), mean position of extreme-, ultra-, and M subdwarfs (crosses), quasars (dots) and unevolved elliptical galaxies (thin colored line) as a function of redshift. *Upper right:* Same as previous figure with the Bruzual & Charlot (2003) single stellar population 5 Gyr evolutionary model for the elliptical galaxies. *Lower left:* g-r/z-y color-color diagram for objects in first figure. See also Figure 10.1 in the AGN chapter.

identified to date, largely serendipitously with 2MASS and SDSS. But with $15 \lesssim M_i \lesssim 18$, they will be detected in substantial numbers with LSST, with volume-complete samples out to at least 200 pc. LSST should also discover specimens of the even cooler T-type subdwarfs, whose spectral properties are as yet unknown but likely to be substantially modified by metallicity effects. Collectively these low-temperature subdwarfs will facilitate the first measurement of the hydrogen-burning gap in the halo luminosity function, a population age indicator that can constrain the formation history of the low-mass halo and its subpopulations (e.g. Burrows et al. 1993).

6.9 Very Low-Mass Stars and Brown Dwarfs in the Solar Neighborhood

Kevin R. Covey, John J. Bochanski, Paul Thorman, Pat Boeshaar, Sarah Schmidt, Eric J. Hilton, Mario Jurić, Željko Ivezić, Keivan G. Stassun, Phillip A. Cargile, Saurav Dhital, Leslie Hebb, Andrew A. West, Suzanne L. Hawley

6.9.1 The Solar Neighborhood in the Next Decade

The least–massive constituents of the Galactic population are brown dwarfs, objects too small to sustain hydrogen fusion in their cores. These are divided into L dwarfs (Kirkpatrick et al. 1999), which have T_{eff} between 1500K and 2200K, whose spectra show weakening of the TiO absorption bands, and T dwarfs with T_{eff} between 800K and 1500K, which show the presence of CH_4 in their atmospheres. An additional spectral type, the Y dwarf (after Kirkpatrick et al. 1999), has been reserved to describe possible dwarfs with even cooler temperatures, which are expected to show NH_3 absorption, a weakening in the optical alkali lines, and a reversal of the blueward $J-K$ trend caused by CH_4 absorption in T dwarfs (Kirkpatrick 2005). Although their masses are low, these brown dwarfs are relatively common in the solar neighborhood, with 600 L and 150 T dwarfs now confirmed. Most of these have been discovered by combining near–infrared imaging (e.g. 2MASS; Skrutskie et al. 2006) with optical surveys (e.g. SDSS; York et al. 2000); the faintness of these objects at optical wavelengths ($M_z > 13$) and the depth of existing NIR imaging are such that these brown dwarfs are overwhelmingly located within the immediate solar neighborhood ($d < 65$ pc). Informing theoretical models of these objects requires measurements of precise physical parameters such as radius and mass.

A number of ongoing or near–term surveys will expand the census of brown dwarfs by 2017, when LSST will begin standard survey operations. The largest single epoch catalog of warm (i.e., L and early T) brown dwarfs will be compiled by the UKIDSS NIR survey (Hewett et al. 2006), which is currently in progress and capable of detecting L0 dwarfs in the J-band within ~ 250 pc. At the cool end, the upcoming WISE mid-IR space telescope (Mainzer et al. 2005) will provide [3.3]-[4.7] μm colors for early T dwarfs within 200 pc (assuming colors and magnitudes from Patten et al. 2006) and all T9 dwarfs within 20 pc, and exquisite sensitivity to cooler Y dwarfs. Multi-epoch photometric surveys enable initial measurements of a source's trigonometric parallax and potential binarity, such that brown dwarfs detected by such surveys have significantly more value for constraining theoretical models. The SkyMapper survey (SSSS Keller et al. 2007), a large-area imaging survey covering the southern sky to depths similar to SDSS, will begin within the next few years. SkyMapper's six-year campaign will produce parallaxes for brown dwarfs within 20 pc. The Pan-STARRS PS1 survey will detect L0 dwarfs in the i band out to 400 pc and measure parallaxes for those within 100 pc; the volume sampled shrinks for fainter, cooler brown dwarfs.

6.9.2 Simulating LSST's Yield of Solar Neighborhood MLTY Dwarfs

Unlike previous surveys, LSST will not depend on separate NIR surveys in order to distinguish L and T dwarfs from possible contaminants such as transient detections, high-redshift quasars, and red galaxies (see Figure 10.6). A narrow range of late L dwarfs may overlap with $z \simeq 6.25$ quasars in color; shortly after the start of the survey, even these brown dwarfs will be identifiable by their proper motions. The addition of the y band allows color identification based on detection in only the three reddest LSST bands, allowing LSST to detect (5 σ in full 10-year co-adds) L0 dwarfs out to 2100 pc, and T0 dwarfs to 100 pc. This L dwarf detection limit extends well into the Thick disk, enabling LSST to probe the physics of old, metal–poor substellar objects (see § 6.7), and potentially decode the star formation history of the thick and thin disks of the Milky Way from the age distribution of field brown dwarfs.

We have constructed a detailed simulation of the very-low mass (VLM) stars and brown dwarfs in the solar neighborhood; using the baseline specifications for the LSST system, we have identified the subsets of this population that LSST will characterize with varying degrees of precision. To model the stellar population in the stellar neighborhood, we have adopted $ugriz$ absolute magnitudes for VLM stars as tabulated by Kraus & Hillenbrand (2007), synthetic $z - y$ colors calculated from optical and infrared template spectra provided by Bochanski et al. (2007) and Cushing et al. (2005), and the mass function and space densities of low-mass stars measured by Bochanski et al. (in preparation).

The lack of a hydrogen-burning main sequence in the brown dwarf regime introduces strong degeneracies into the relationships between the masses, ages, and luminosities of substellar objects. These degeneracies are an important consideration for studies of the properties of field brown dwarfs, as the properties of brown dwarfs in the solar neighborhood are sensitive to the star formation history of the Milky Way and the shape of the stellar/substellar mass function. We are currently developing simulations that explore the brown dwarf samples LSST would observe assuming different star formation histories and mass functions; for simplicity, however, the simulations described below assume a single population of 3 Gyr brown dwarfs. In detail, this substellar population is described by:

- For $2100 > T_{eff} > 1200$ (L dwarfs and the earliest Ts) we adopt empirical SDSS riz magnitudes (Schmidt et al. in preparation), supplemented by synthetic ugy magnitudes from cloudy Burrows et al. (2006) models.
- For $1200 > T_{eff} > 600$ (mid-late Ts), we adopt synthetic $ugrizy$ magnitudes calculated from cloud-free Burrows et al. (2006) models.
- For $T_{eff} > 600$ (as yet undiscovered Y dwarfs), we adopt synthetic $ugrizy$ magnitudes calculated from the ultra-cool Burrows et al. (2003) models.
- We adopt the Cruz et al. (2007) luminosity function for L dwarfs; for T and Y dwarfs, we define a luminosity function with a linear extrapolation anchored by the coolest bin of the

Table 6.4: LSST's MLTY Dwarf Sample

Spectral Class	N_{rizy}	N_{izy}	N_{zy}	N_{π}
M	>347,000	>347,000	>347,000	>347,000
L	18,500	27,500	35,600	6,550
T	∼3-4	50	2,300	∼260
Y	0	0	∼18	∼5

Cruz et al. luminosity and the empirical T dwarf space density measured by Metchev & Hillenbrand (2007).

Using the above parameters as inputs, we simulated the properties of field stars and brown dwarfs within 200 pc of the Sun. Table 6.4 summarizes the number of stars and brown dwarfs LSST will likely detect in various filter combinations as a function of spectral type with reliable parallaxes, to the single-visit depth. To make this estimate, we assume the relationship between parallax uncertainty vs. r band magnitude reported in Table 3.3, but we increase these uncertainties by a factor of 1.25 to reflect that many stars and brown dwarfs will lack u and g band detections.

These results indicate that LSST will greatly expand the sample of ultra–cool objects with reliable parallax measurements. These extremely red objects are ill-suited for parallax measurements with Gaia's blue filterset, while LSST's greater depth and astrometric precision will enable it to measure parallaxes for brown dwarfs significantly beyond the parallax limit of Pan-STARRS. This sample will, therefore, provide a key set of well-characterized brown dwarfs which can confront the predictions of theoretical models of brown dwarf and planetary atmospheres.

While we focus here primarily on brown dwarfs in the Galactic field, we also note that LSST's deep photometric limits and its ability to select cluster members via high-precision proper motions will provide a high-fidelity census of the very-low-mass populations of many Southern open clusters. LSST will be able to easily identify VLM objects near or below the hydrogen-burning limit in most of the clusters listed in Tables 6.1 and 6.2, with ages ranging from 1 Myr to ∼10 Gyr and to distances as far as ∼1.5 kpc. LSST will provide colors and magnitudes for a large sample of L and T dwarfs with ages and metallicities derived from the morphology of each cluster's upper main sequence. This sample will define empirical brown dwarf cooling curves over a wide range of ages, providing a key calibration for understanding the properties of nearby field brown dwarfs whose ages are almost entirely undetermined.

6.9.3 Science Results

Measuring Fundamental Physical Parameters of VLM stars and Brown Dwarfs

The wide areal coverage, depth, precision, and temporal coverage of LSST photometry make it an ideal instrument for the detection and characterization of low–mass ($M < 0.8M_{\odot}$) eclipsing binaries within the Milky Way. Currently, only ~ 15 low–mass eclipsing binaries are known (Demory et al. 2009), and even fewer VLM binaries, presumably due to their intrinsic faintness ($L < 0.05\,L_{\odot}$ for a $0.4M_{\odot}$ early M dwarf) and a stellar binary fraction that decreases with mass (Duquennoy &

Mayor 1991; Burgasser et al. 2007). The large volume probed by LSST, with typical low-mass pairs being detected at $d < 200$ pc, will discover a slew of these rare systems.

To quantify the expected yield of VLM star and brown dwarf EBs, we start with the expected yield of MLTY dwarfs from the N_{zy} column of Table 6.4. Such objects will already have LSST light curves in the z and y bands, which can be complemented by follow-up light curves in the JHK bands. A five-band light curve analysis is sufficient for modeling the EB parameters to $\sim 1\%$ (e.g. Stassun et al. 2004). Assuming that approximately 1/10 of the M dwarfs are M9 brown dwarfs, then the total brown dwarf yield from Table 6.4 is $\sim 70,000$. Recent surveys of binarity among brown dwarfs yield fractions of 10–15% for visual binaries with separations of > 1 AU (e.g., Martín et al. 2003; Bouy et al. 2003). Thus a very conservative estimate for the overall binary fraction of brown dwarfs is 10%. Next, assuming a distribution of binary separations similar to that for M dwarfs (Fischer & Marcy 1992) implies that $\sim 10\%$ of these will be tight, spectroscopic binaries with physical separations < 0.1 AU. Finally, among these, the probability of an eclipse is of order $(R_1 + R_2)/a$, where R_1 and R_2 are the component radii and a is the semi-major axis, so for two brown dwarfs each with $R \sim 0.1\ \mathrm{R}_\odot$ and $a \sim 0.1$ AU, we have an eclipse probability of $\sim 1\%$. Thus the overall expected brown dwarf EB yield will be $0.1 \times 0.1 \times 0.01 \times 70,000 \approx 7$. With only one brown dwarf EB currently known (Stassun et al. 2006, 2007), the LSST yield represents a critical forward advance for substellar science. The calculation above implies an overall yield of ~ 40 VLM eclipsing binary systems, a factor of several increase over the number currently known.

These fundamental astrophysical laboratories will redefine the empirical mass–radius relations, for which current data are sparse and derived from heterogeneous sources. For nearby eclipsing systems, native LSST parallaxes will result in model–free luminosity estimates, and can help constrain the effective temperature distribution of low–mass stars. This will be especially important at smaller masses ($M < 0.1 M_\odot$), where only one eclipsing binary is known (Stassun et al. 2006)[1]. This regime will be well suited to LSST's survey specifications and complement the Pan-STARRS survey as LSST will be probing a different area of the sky (the Southern Hemisphere). At large distances, the currently elusive halo binaries, identified kinematically through proper motions, may serve as probes for changes in low–mass stellar structure due to metallicity. Low–mass stars inhabit an interesting regime in stellar structure. At masses $\sim 0.4 M_\odot$, the interiors of low–mass stars transition from a convective core surrounded by a radiative shell to a fully convective interior. Observations do not currently constrain how metallicity may affect this transition, and only the deep photometry that LSST will provide will enable an empirical investigation of this phenomenon. The eclipsing binaries discovered in LSST will enable new science and redefine the empirical understanding of stellar structure and binary properties. With the "brown dwarf desert" significantly limiting the existence of F/G/K+brown dwarf binaries[2], VLM+brown dwarf eclipsing binaries are the only systems in which masses and radii of brown dwarfs can be measured—along with their temperatures.

High-resolution near-infrared spectroscopic follow-up on 10-m class telescopes will be critical for determining the radial velocity orbit solutions for the discovered eclipsing binaries. For example, the one known brown dwarf eclipsing binary (Stassun et al. 2006, 2007) is in the Orion Nebula

[1] This system exhibits interesting behavior: the hotter component (primary) is actually fainter than its companion.

[2] For example, Grether & Lineweaver (2006) find that approximately 16% of solar-type stars have companions with $P < 5$ yr, $M > 1\ \mathrm{M}_{Jup}$. Of these, $4.3 \pm 1.0\%$ have companions of planetary mass, 0.1% have brown dwarf companions, and $11.2 \pm 1.6\%$ have companions of stellar mass.

cluster at a distance of ~ 500 pc, the outer limit for the systems included in the estimated yields calculated above. Its radial velocity curve was obtained with the *Phoenix* spectrograph on the Gemini South 8-m telescope operating in the H band (1.5 μm).

Variability of VLM Stars and Brown Dwarfs

The temporal coverage of LSST opens a window on the time variability of VLM stars, including flares, spot modulation, and rotation periods. Additionally, by discovering new eclipsing binaries, LSST will provide new laboratories for measuring fundamental stellar parameters like mass and radius.

Stellar magnetic activity has been observed and studied on M dwarfs for several decades (see § 8.9.1 for a review of this subject), but much less is known about activity on brown dwarfs. The fraction of stars with Hα in emission, an indicator of magnetic activity, peaks around M7 and decreases through mid-L (Gizis et al. 2000; West et al. 2004; Schmidt et al. 2007; West et al. 2008) although the changing continuum level with spectral type makes this an imperfect tracer of magnetic field strength. Burgasser et al. (2003b) report three T dwarfs with Hα activity, one of which has strong, sustained emission (Burgasser et al. 2002). Flares on brown dwarfs appear to be less frequent than on M dwarfs, but have been seen in both X-ray (Rutledge et al. 2000) and radio (Berger et al. 2001). Optical spectra have shown variable Hα emission in L dwarfs (Hall 2002; Liebert et al. 2003; Schmidt et al. 2007; Reiners & Basri 2008) that may be the result of flares. LSST's new observations of such a large number of brown dwarfs over dozens of epochs will provide much–needed empirical determinations of flare rates.

LSST's temporal coverage will permit precise, dense coverage of most main sequence stars with spots. This subject is modeled in detail in § 6.6, and discussed below in the context of low–mass stars and brown dwarfs. Starspots, analogous to their solar counterparts, provide a measure of the relative magnetic field strength for stars of a given spectral type (and mass), assuming that the spot coverage is not so uniform as to prevent rotational modulation of the star's observed flux. If spot variations can be detected, the *ugrizy* light curves of these stars can be used to estimate temperature, from relative depths due to spot modulation, and filling factors, from the absolute deviations from a pristine stellar photosphere.

Furthermore, the photometric signatures imprinted by these cooler regions provide the opportunity to measure rotation periods that are shorter than the lifetime of a typical starspot (∼weeks to months). As demonstrated in § 6.6, LSST will be adept at measuring the rotation periods of coherently spotted, magnetically active, low–mass stars. Combining the measured rotation periods with other proxies of stellar magnetic activity will provide a fundamental test of magnetic dynamo generation theory. This is particularly interesting within the low–mass regime. At masses $\sim 0.4 M_{\odot}$, the interior of low–mass stars transition from an convective core surrounded by a radiative shell to a fully convective interior. The transition region between convective core and radiative exterior is thought to drive magnetic activity in earlier type low–mass stars (West et al. 2008).

Substellar Subdwarfs

The deep LSST survey imaging will photometrically identify statistically significant numbers of L dwarfs at large distances from the Galactic plane. These dwarfs will allow the spatial distribution of dwarfs in the thin and thick disk populations to be determined, and allow a search for additional members of a halo population of metal–poor subdwarf brown dwarfs to be discovered (e.g., Cushing et al. 2009). The kinematics of the L dwarf and subdwarf populations will also provide an empirical test of the metallicity dependence of the hydrogen burning limit, based on the model cooling curves. The existence of a population of substellar subdwarfs may also indicate star formation due to infalling primordial gas, or be a relic of the Milky Way's recent merger history.

6.10 Eclipsing Variables

Andrej Prša, Keivan G. Stassun, Joshua Pepper

The importance of eclipsing binary stars (EBs) can hardly be overstated. Their analysis provides:

- **Calibration-free physical properties of stars (i.e., masses, radii, surface temperatures, luminosities).** Masses are measured dynamically via radial velocities with no $\sin i$ ambiguity because the eclipses provide an accurate measure of $\sin i$. Radii are measured directly from the eclipse durations, the temperature ratio from the eclipse depths. The radii and temperatures together yield the luminosities.
- **Accurate stellar distances.** With luminosities measured directly from the component radii and temperatures, the distance to the EB follows directly from the observed fluxes.
- **Precise stellar ages.** By comparing the measured mass-radius relationship with stellar evolution models, precise stellar ages can be determined. The accuracy of the age determination is of course model dependent and also mass dependent, with typical accuracy of $\sim 5\%$ for $M_\star > 1.2$ $M_\odot$ and $\sim 50\%$ for $M_\star < 0.8$ $M_\odot$ (Stassun et al. 2009).
- **Stringent tests of stellar evolution models.** With accurate, directly determined properties of the two stars in the EB, the basic predictions of stellar evolution models can be tested. For example, the two stars should lie on a single model isochrone under the assumption that they formed together as a binary, or the observed parameter relationships (mass-radius, temperature-luminosity, and so on) can be compared against the model predictions.

The products of state-of-the-art EB modeling are seminal to many areas of astrophysics:

- calibrating the cosmic distance scale;
- mapping clusters and other stellar populations (e.g., star-forming regions, streams, tidal tails, etc) in the Milky Way;
- determining initial mass functions and studying stellar population theory;
- understanding stellar energy transfer mechanisms (including activity) as a function of temperature, metallicity, and evolutionary stage;
- calibrating stellar color-temperature transformations, mass-radius-luminosity relationships, and other relations basic to a broad array of stellar astrophysics; and

Table 6.5: Distance Limits for LSST Detection of Sample EBs.

Sample Binary[a] Type	Binary Absolute Magnitude	Distance[b] for $r = 22.0$ [kpc]	Distance[b] for $r = 19.5$ [kpc]
M5V + M5V	12.9	0.7	0.2
M2V + M2V	9.0	4.0	1.3
K0V + K0V	5.0	25.1	7.9
G2V + MxV	4.6	30.2	9.5
G5III + GxV	2.9	66.1	20.1

[a]Scientifically interesting EB systems. EBs with M-dwarf components are rare in the literature. Their discovery will permit detailed testing of stellar models in this important mass regime. G-dwarf/M-dwarf pairs will be particularly valuable for pinning down the properties of M-dwarfs, since the temperature scale of G-dwarfs is relatively well established. A particularly exciting prospect are Cepheids (G giants) in EB systems.

[b]Assuming no extinction.

- studying stellar dynamics, tidal interactions, mass transfer, accretion, chromospheric activity, etc.

LSST will be ideally suited for extensive mapping of EBs. As the simulations described below demonstrate, LSST will detect essentially all EBs with orbital periods less than 0.3 days, and 50% of those with periods up to ∼10 days (see Figure 6.13). This completeness estimate is based on analysis of a single passband; simultaneous analysis of all six LSST bands will in reality improve this completeness. With a nominal detection limit of $r = 24.5$, a magnitude of $r = 22.0$ should allow detection of targets with a S/N of 3.5, $r = 19.5$ will have S/N of 10 per data point. Table 6.5 shows the distance out to which certain fiducial EB types can be detected. For example, a pair of eclipsing M2 dwarfs will be detected out to 1 kpc with S/N of 10.

We can estimate the number of EBs that LSST will be able to fully characterize (our experience modeling EB light curves shows that $S/N \sim 3.5$ per data point typically suffices for the determination of physical and geometric parameters to a few percent). Gaia will observe ∼1 billion stars down to $r \sim 20.5$ over the whole sky. We can expect that LSST will observe ∼0.5 billion stars to this same depth in the southern hemisphere. Extrapolating the results from Hipparcos (917 EBs in the sample of 118,218 observed stars; or 0.8%), the LSST sample will contain ∼16 million EBs down to $r \sim 22.0$. The average detection rate for EBs over all periods will be around 40% (∼ 100% for $P < 0.3$ days, ∼50% for $P \sim 10$ days, ∼ 20% for $P < 30$ days; Figure 6.13), bringing the total number to ∼6.4 million EBs. Roughly 25% of those will have components of similar luminosities (double-lined systems), yielding ∼1.6 million EBs with S/N≥ 10 for ready detailed modeling.

6.10.1 Simulating LSST's Harvest of Eclipsing Binary Stars

With LSST's six-band photometry and a cut-off magnitude of $r \sim 24.5$, the limiting factor for the detection of EB stars will be the cadence of observations. To estimate LSST's EB detection efficiency, we set up a test-bed by employing PHOEBE (Prša & Zwitter 2005), a Wilson & Devinney (1971) based eclipsing binary modeling suite. We first partitioned the sky into 1558 fields, covering all right ascensions and declinations between −90° and 10°. The cadence of observations of these fields was then determined from the Simulated Survey Technical Analysis Report (SSTAR) for the operations simulations described in § 3.1.

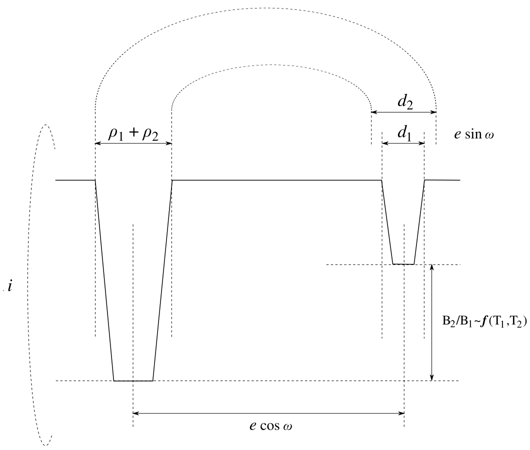

Figure 6.12: Schematic view of an EB light curve. Surface brightness ratio B_2/B_1 directly determines the ratio of depths of both eclipses, and can be roughly approximated by the temperature ratio T_2/T_1. The sum of fractional radii $\rho_1 + \rho_2$ determines the baseline width of the eclipses, while $e \sin \omega$ determines the ratio between the widths of each eclipse, d_1 and d_2. The phase separation of the eclipses is governed by $e \cos \omega$, and the overall amplitude of the light curve, as well as the shape of eclipses, are determined by $\sin i$.

To estimate LSST detection effectiveness, we synthesized light curves for five EBs that are representative of the given morphology type: well detached, intermediate detached, close detached, close, and contact. These most notably differ in fractional radii and orbital periods, hence in the number of observed data points in eclipses. Each EB light curve is described by its ephemeris (HJD_0 and period P_0) and five principal parameters: T_2/T_1, $\rho_1 + \rho_2$, $e \sin \omega$, $e \cos \omega$ and $\sin i$ (cf. Figure 6.12; for a thorough discussion about the choice of principal parameters please refer to Prša et al. 2008).

Let N_1 and N_2 be the numbers of data points observed in each eclipse. To detect and correctly classify light curves, we need as many points in *both* eclipses as possible. We thus selected the product $\mathcal{C} = N_1 N_2$ for the cost function. This way, if all data points are observed during one eclipse but not the other, this quantity will be zero. Consecutive observations of long period EBs present another complication: although they contribute equally to the in-eclipse count, they cover essentially the same point in phase space because of the prolonged duration of eclipses. To account for that, all adjacent data points in phase space that are separated by less than some threshold value – in our simulation we used 1/1000 of the period – are counted as a single data point.

The cost function $\mathcal{C}$, shaped according to these insights, was computed for all five synthesized EBs (the details of the study are presented in Prša et al. 2009). The light curves are computed in phase space, assuming that periodicity can be found correctly by a period search algorithm if the S/N of a single data point exceeds 3.5 (or, in terms of LSST, $r < 22.0$). Simulation steps are as follows:

1. given the P_0, pick a random phase shift between 0.0 and 1.0 and convert the time array to the phase array;
2. sort the array and eliminate all data points with adjacent phases closer than the threshold value required to resolve them;
3. given the $\rho_1 + \rho_2$, count the number of data points in eclipses (N_1, N_2);
4. compute the cost function value $\mathcal{C} = N_1 N_2$;

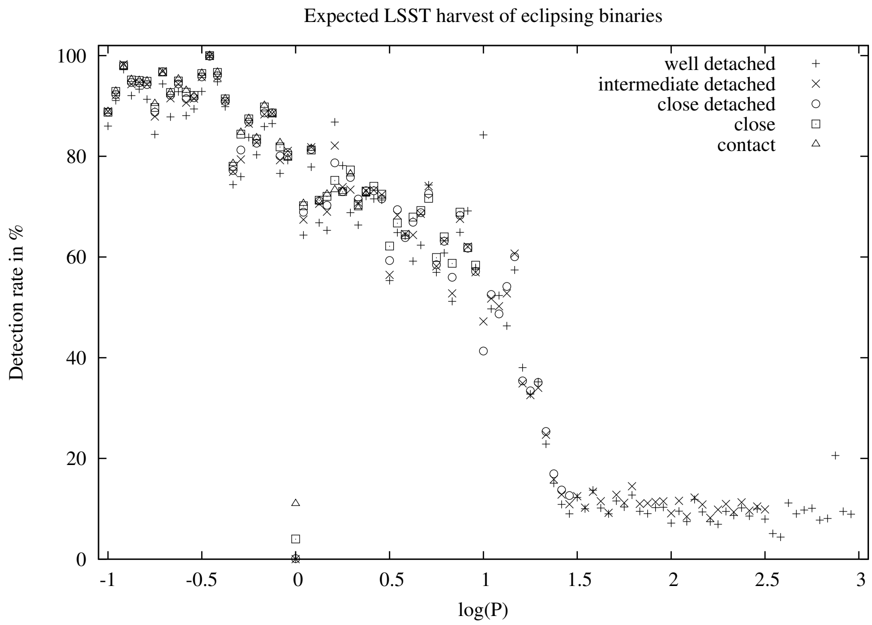

Figure 6.13: The detection rate of eclipsing binary stars based on their morphology and their orbital period. Assuming that S/N$\geq$ 3.5 per data point suffices for reliable recovery of orbital periods, LSST will detect almost all short period EBs, around 50% of intermediate EBs, and around 10% of long period EBs down to $r \sim 22.0$. The simulation is based on a single passband, implying that the values quoted here correspond to the worst case scenario. Since short and intermediate period EBs are most interesting for stellar population studies, it is clear that the expected LSST harvest of EB stars will be unprecedented.

5. repeat steps 1-4 for a predefined number of times (say, 100), and find the average value of $\mathcal{C}$;
6. repeat steps 1-5 for all 1588 fields (α_i, δ_i); and
7. repeat steps 1-6 for a range of periods sampled from a uniform distribution in $\log(P_0) \in [-1, 3]$.

Figure 6.13 depicts the results of our simulation. Under the assumption that the variability analysis provides correct periods, the LSST sample of short period eclipsing binary stars will be essentially complete to $r \sim 24.5$; these stars have the best characteristics to serve as calibrators – both because of their physical properties and because of the feasibility for the follow-up studies.

6.10.2 Effectiveness of EB Parameter Determination from LSST Data

To further qualify LSST's harvest of EBs, we generated a sample of 10,000 light curves across the southern sky, using the cadence coming out of the Operations Simulations (§ 3.1). The values of principal parameters were sampled randomly, according to the following probability distribution functions:

- T_2/T_1 is sampled from a normal distribution $\mathcal{G}(1.0, 0.18)$;
- P_0 is sampled from a log-uniform distribution $[-1, 4]$;

- $\rho_1+\rho_2$ is sampled from a uniform distribution $[0.05, \delta_{\rm max}-0.05]$, where $\delta_{\rm max}$ is the morphology constraint parameter that depends exponentially on the value of $\log P_0$:

$$\delta_{\rm max}(\log P_0) = 0.7 \exp\left(-\frac{1+\log P_0}{4}\right);$$

- The eccentricity e is sampled from an exponential distribution $\mathcal{E}(0.0, \epsilon_{\rm max}/2)$, where $\epsilon_{\rm max}$ is the attenuation parameter that depends exponentially on the value of $\rho_1 + \rho_2$:

$$\epsilon_{\rm max} = 0.7 \exp\left(-\frac{\rho_1+\rho_2-0.05}{1/6}\right);$$

- The argument of periastron ω is sampled from a uniform distribution $[0, 2\pi]$; the combination of the e and ω distributions produces a sharp, normal-like distribution in $e \sin\omega$ and $e\cos\omega$;
- The inclination i is sampled from a uniform distribution $[i_{\rm grazing}, 90°]$, where $i_{\rm grazing}$ is the inclination of a grazing eclipse.

Once the light curve sample was created, we added random Gaussian errors with σ ranging from 0.001 to 0.2 (simulating different distances and, hence, different S/N), and we measured best fit parameters with `ebai` (Eclipsing Binaries via Artificial Intelligence; Prša et al. 2008), an efficient artificial intelligence based engine for EB classification via trained neural networks. Backpropagation network training, the only computationally intensive part of `ebai`, needs to be performed only once for a given passband; this is done on a 24-node Beowulf cluster using OpenMPI. Once trained, the network works very fast; 10,000 light curves used in this simulation were processed in 0.5 s on a 2.0GHz laptop, where most of this time was spent on I/O operations.

Figure 6.14 depicts the results of `ebai`: 80% of all stars passed through the engine have less than 15% error in *all five parameters*. A 15% error might seem large at first (typical error estimates of state-of-the-art EB modeling are close to 2-3%), but bear in mind that `ebai` serves to provide an *initial* estimate for parameter values that would subsequently be improved by model-based methods such as Differential Corrections or Nelder & Mead's Simplex, as implemented in `PHOEBE`.

These two simulations indicate LSST will provide a sample of short period EBs (< 1 day) essentially complete to $r \sim 22.0$; a sample of EBs with periods of tens of days will be ~50% complete; a sample of long-period EBs will be ~10% complete. Since short period EBs carry the most astrophysical significance, and since parameter determination is most accurate for those stars because of the large number of data points in eclipses, LSST's high detection efficiency and accurate parameter measurements promise to revolutionize EB science and the many fields that EBs influence.

6.11 White Dwarfs

Jason Kalirai, Charles F. Claver, David Monet, Željko Ivezić, J.B. Holberg

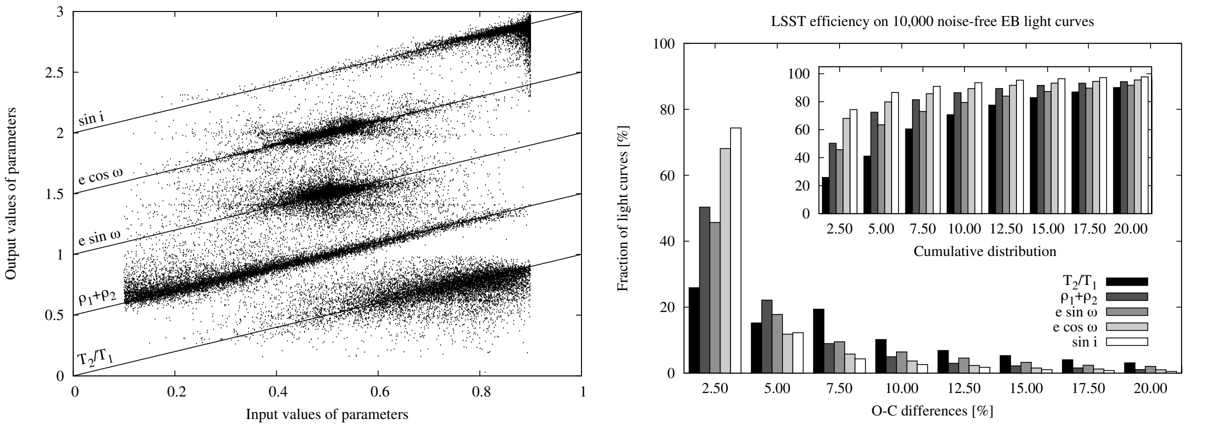

Figure 6.14: *Left:* comparison between input and `ebai`-computed values of orbital parameters in a simulation of LSST-observed eclipsing binaries. For neural network optimization purposes, parameter values were rescaled to the interval $[0.1, 0.9]$. Successive parameters are vertically offset by 0.5 and correlation guidelines are provided to facilitate comparison. *Right:* histogram of the residuals computed by `ebai`. Parameter T_2/T_1 is most weakly determined (26% of all light curves have a corresponding error less than 2.5%) – this is due to the only approximate relationship between T_2/T_1 and the surface brightness ratio B_2/B_1. Parameters $\sin i$ and $e\cos\omega$ have the highest success rate (75% and 68% of all light curves have $\sin i$ and $e\cos\omega$, respectively, determined to better than 2.5%), meaning that the cadence suffices for accurate determination of orbital properties. The inset depicts the cumulative distribution of the residuals: over 80% of the sample has errors in *all* parameters less than 15%.

6.11.1 The Milky Way White Dwarf Population

Over 97% of all stars end their lives passively, shedding their outer layers and forming low mass white dwarfs. These stellar cinders are the burnt out cores of low and intermediate mass hydrogen burning stars and contain no more nuclear fuel. As time passes, white dwarfs will slowly cool and release stored thermal energy into space becoming dimmer and dimmer. Although they are difficult to study given their intrinsic faintness, successful observations of white dwarfs can shed light on a very diverse range of astrophysical problems.

The largest sample of white dwarfs studied to date comes from SDSS, which has increased the known population of these stars by over an order of magnitude to more than 10,000 stars (Eisenstein et al. 2006). This has enhanced our knowledge of stellar chemical evolution beyond the main sequence, uncovered new species of degenerate stars such as highly magnetized white dwarfs and accretion disk objects that may harbor planets, and provided a more accurate white dwarf luminosity function for the Galactic disk (Harris et al. 2006).

The luminosity function of white dwarfs rises with increasing photometric depth, such that LSST's sensitivity and wide areal coverage is expected to yield over 13 million white dwarfs with $r < 24.5$ and over 50 million to the final co-added depth (model luminosity functions are presented later). LSST will completely sample the brightest white dwarfs in our Galaxy (with $M_V \sim 11$) to 20 kpc and beyond. This broadband study of white dwarfs will yield important leverage on the overall baryon mass budget of the Milky Way and provide an unprecedented sample of white dwarfs, of all spectral types, to improve our understanding of a variety of astrophysical problems. For example, based on MACHO predictions, LSST will be sensitive to thousands of dark halo white dwarfs and can therefore verify or rule out whether an appreciable fraction of the Galactic dark matter is tied

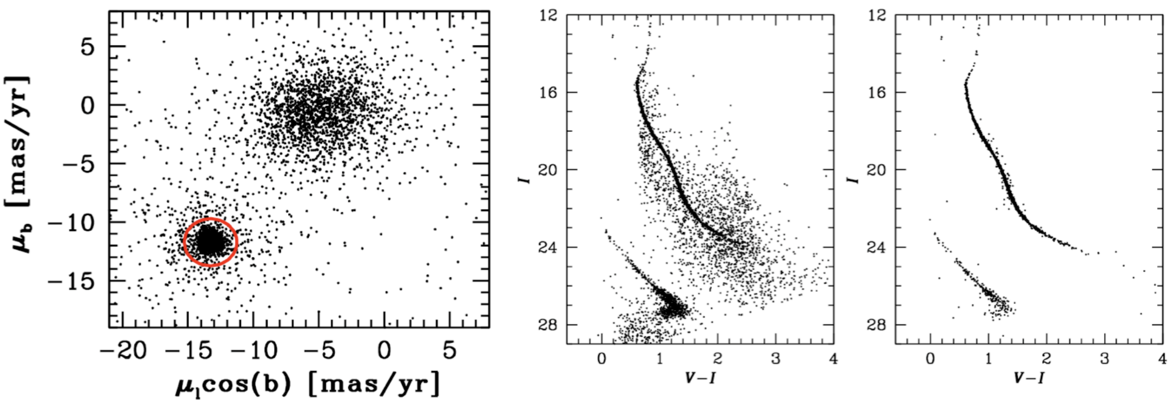

Figure 6.15: The color-magnitude diagram of NGC 6397 from HST observations with ACS (Richer et al. 2008) based on all stars (center) and proper motion members over a fraction of the field (right). The proper motion diagram (left) illustrates the motion of the cluster with respect to the field, over a 10 year baseline. The rich white dwarf cooling sequence of the star cluster (faint-blue end) is modeled in Hansen et al. (2007) to yield an independent age for the cluster of $t = 11.5 \pm 0.5$ Gyr.

up in these stars (Alcock et al. 2000). LSST's photometry of white dwarfs will also be more than three times as precise as SDSS photometry, particularly in the u band, which is often definitive for these stars. This greatly facilitates the matching of observed colors with predicted colors at the 1% level making it possible to estimate white dwarf temperatures, gravities, and spectral types over a much wider range of parameter space then is now practical. Below we outline several of the key science cases that LSST will address, followed by a specific discussion of the simulated distribution of white dwarfs that LSST will be sensitive to.

6.11.2 White Dwarfs as Chronometers – Dating Stellar Components of the Milky Way

Although SDSS found abundant white dwarfs in the Galactic disk, the survey was too shallow to uncover large numbers of halo white dwarfs. These distant objects, which LSST will detect, will allow for the first time the construction of a luminosity function for field *halo* white dwarfs (see § 6.11.6 for the expected white dwarf spatial distribution). The structure in this luminosity function (and in particular, the turnover at the faint end) holds important clues about the formation time of each specific Galactic component because the white dwarfs cool predictably with time. Therefore, an older population of white dwarfs is expected to show a fainter turnover as the stars have had more time to cool. As we show in § 6.11.6, a simulation of the expected LSST white dwarf number counts indicates that over 400,000 halo white dwarfs will be measured to $r < 24.5$.

The faintest white dwarfs in the nearest globular star clusters have now been detected with HST (see Figure 6.15); at $M_V \gtrsim 16$ (Hansen et al. 2007), they are a full magnitude fainter than their counterparts in the Galactic disk (Harris et al. 2006). This work provides independent age measurements for nearby globular clusters and suggests that these objects formed several Gyr before the Galactic disk. By extending these studies to the remnants in the Milky Way field halo, LSST will provide us with a direct measurement of the age of the Galactic halo, a vital input into the construction of Galactic formation models. These measurements can not only help answer when our Galaxy formed, but also constrain the formation timescales of different populations within the same component. For example, the age distribution of Milky Way globulars can be contrasted with the field halo population to shed light on the formation processes of the clusters themselves (e.g., in situ formation vs. accretion).

LSST will also improve, by several orders of magnitude, the statistics of the field Milky Way disk white dwarf luminosity function. Harris et al. (2006) comment on the lack of a precise ($\sigma \sim$ 2 Gyr) age measurement (Leggett et al. 1998; Hansen et al. 2002) given the low numbers of low-luminosity white dwarfs in the SDSS sample. LSST will not only constrain the age of the oldest stars in the Galactic disk to a much higher accuracy than currently possible, but also map out the complete star formation history of the disk. Epochs of enhanced star formation in the Galactic disk's history will leave imprints on the white dwarf luminosity function in the form of brighter peaks. The luminosity and width of these peaks can be inverted to shed light on the formation time and timescale of the star forming events. In § 6.11.6 we simulate the expected LSST white dwarf disk luminosity function.

A key component of LSST's study of Milky Way white dwarfs will be a kinematic analysis. With LSST we will look for dependencies of the white dwarf luminosity function in the disk with the population's velocity, and therefore verify the age difference between the thin and thick disks. The velocity may also be correlated with other Galactic parameters, such as metallicity, to give indirect age-metallicity estimates. Alternatively, dependencies of the luminosity function (and, therefore, age) may exist with scale height above/below the Galactic plane, improving our understanding of Galactic structure. The expected kinematic separation of these populations, based on LSST statistics, is also discussed near the end of this chapter.

6.11.3 White Dwarfs in Stellar Populations

The comparison of theoretical isochrones to observational color-magnitude diagrams has historically been used to infer the age of a nearby stellar population, provided that the distance is known through independent methods (e.g., main sequence fitting with the Hyades cluster, for which individual parallax measurements exist). In practice this comparison is often limited by our lack of knowledge of fundamental quantities (e.g., the distance and metallicity) and so the isochrones are used to estimate multiple parameters at once. When combined with the uncertainties in the microphysics of the models (e.g., the role of gravitational settling or the treatment of convective core overshooting), the absolute uncertainty on the age of any stellar population using the main sequence turn-off method is ∼2 Gyr for old stellar populations (D'Antona 2002). At higher redshifts, the theoretical isochrones are used to interpret light from distant galaxies in terms of the properties of the systems (e.g., age and metallicity). These age and metallicity measurements form a major component of our understanding of galaxy formation and evolution.

The study of white dwarfs with LSST will naturally extend to stellar populations such as nearby star clusters (§ 6.5). LSST will detect the tip of the white dwarf cooling sequence in star clusters located over 20 kpc from the Sun. It will also completely map the entire white dwarf cooling sequence in nearby globular and open clusters. For example, the faintest white dwarfs in a cluster with $t = 1$ Gyr have $M_V = 13$, and will be seen out to 8 kpc. The white dwarf cooling sequences of these clusters provide age and distance measurements (Hansen et al. 2007). This age measurement

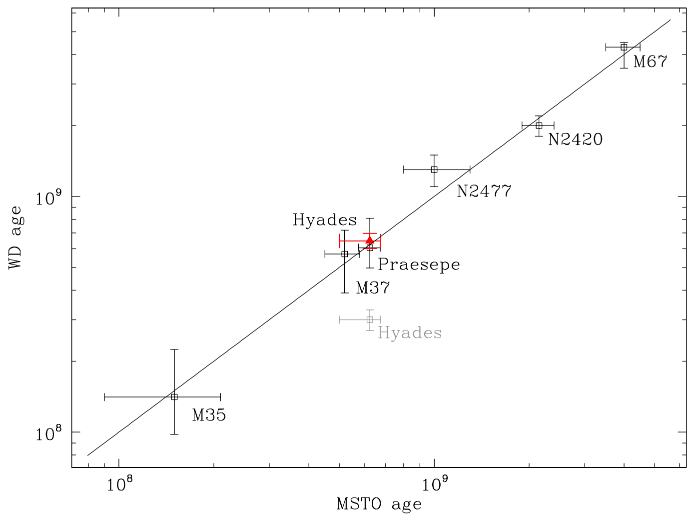

Figure 6.16: The white dwarf cooling ages of several nearby solar metallicity open star clusters are compared with their corresponding main sequence turn-off ages based on a set of theoretical isochrones. The two independent age measurements are in good agreement with one another for the assumed models and would not agree if for example, core-overshooting was not allowed. Taken from DeGennaro et al. (2009).

is not affected by our knowledge of rotation, diffusion, overshooting, even metallicity, and is, therefore, independent of the main sequence turn-off approach. By fixing the age and distance of the stellar population using white dwarf cooling theory, we will be able to test stellar evolution models in exquisite detail and constrain many of the microphysics. These improved models will directly impact our ability to deconvolve the colors of distant galaxies using population synthesis methods.

In Figure 6.16, we compare the main sequence turn-off age with the white dwarf cooling age for the handful of open star clusters where both measurements exist (DeGennaro et al. 2009, in preparation). This work has already shown that synthetic color-magnitude diagrams, based on various sets of theoretical isochrones, that do not adopt convective core-overshooting yield ages are too low to fit the white dwarf cooling measurements (Kalirai et al. 2001b; Kalirai & Tosi 2004). LSST will increase the sample of clusters in which these measurements exist by over an order of magnitude, and thus allow these comparisons to be made over a substantial range in age and metallicity to test a broad region of parameter space in the models.

6.11.4 White Dwarfs as Probes of Stellar Evolution

As an intermediate or low mass star evolves off the main sequence and onto the red giant and asymptotic giant branch, it quickly sheds its outer layers into space. The mass loss mechanisms (e.g., helium flash and thermal pulses on the asymptotic giant branch) are poorly understood theoretically (Habing 1996) and observational constraints are rare given the very short lifetimes of stars in these phases ($\sim 10^5$ years) and heavy obscuration by dusty shells. The end products of this stellar evolution are white dwarfs, and studying these stars in detail beyond the initial imaging observations can directly constrain the total integrated stellar mass loss.

As a follow up study to the initial imaging observations that LSST will undertake, the brightest (i.e., youngest) white dwarfs in nearby stellar populations can be spectroscopically measured with multi-object technology on 8 – 10-m ground-based telescopes (and possibly with TMT or GMT). The spectra of the DA white dwarfs are remarkably simple, showing pressure broadened Balmer lines caused by the thin hydrogen envelope in the atmosphere of the stars. These Balmer lines can be easily modeled to yield the temperature and gravity of the stars, and, therefore, the individual stellar masses (Bergeron et al. 1995). These mass measurements can be uniquely connected to the initial mass of the progenitor star for each white dwarf (e.g., the total cluster age is the sum of the white dwarf cooling age and the main sequence lifetime of the progenitor), and, therefore, an initial-to-final mass relation can be constructed as shown in Figure 6.17 (Kalirai et al. 2008).

LSST will revolutionize our study of the initial-to-final mass relation. The new relation, consisting of hundreds of data points over the full range in initial mass of stars that will form white dwarfs, will directly constrain the amount of mass loss that occurs through stellar evolution. This forms a powerful input to chemical evolution models of galaxies (including enrichment in the interstellar medium) and, therefore, enhances our understanding of star formation efficiencies in these systems (Somerville & Primack 1999). Moreover, LSST will provide new insights into how stellar evolution and mass loss rates are affected by metallicity variations. Theoretically it is expected that mass loss rates in post main sequence evolution depend on metallicity (e.g., see Kalirai et al. 2007, and references therein). These dependencies can be directly tested by constructing relations specifically for clusters of different metallicities that LSST will observe.

LSST's detection of white dwarfs in the youngest stellar systems will also provide new insights into the threshold mass that separates white dwarf production from type II SNe formation. For example, the most massive singly evolved white dwarf that can be connected to a progenitor mass in Figure 6.17 is currently the Pleiades star, which has $M_{\rm initial} = 6.5\ M_\odot$. However, the remnant star of this progenitor is 1.0 $M_\odot$, much smaller than the Chandrasekhar limit, suggesting that more massive *singly* evolving white dwarfs remain to be found in star clusters. Theoretically, this threshold mass is difficult to constrain as models do not include rotation and are very sensitive to overshooting and rotationally induced mixing. A shift in the critical mass from 9 $M_\odot$ (as suggested by an extrapolation of the present initial-final mass relation above) to 6 $M_\odot$ (as suggested by several models for the ignition of carbon in the core of the star, e.g., Girardi et al. 2000) results in a 80% increase in the numbers of type II SNe based on a Salpeter mass function. This changes the amount of kinetic energy imparted into the inter-galactic medium (IGM) and would, in fact, be in better agreement with some observations of the IGM (Binney 2001) as well as the mass function of stars in the solar neighborhood (van den Bergh & Tammann 1991). Such an effect should be seen as a steepening of the initial-final mass relation at higher masses, which LSST will probe by sampling white dwarf populations in successively younger systems. For example, LSST's detection of white dwarfs in a cluster of age 50 Myr, where 8 $M_\odot$ stars are still burning hydrogen on the main sequence, would suggest that the critical mass is above 8 $M_\odot$. Such young open clusters do exist in the southern hemisphere but lack current deep imaging data (e.g., NGC 2451 and NGC 2516).

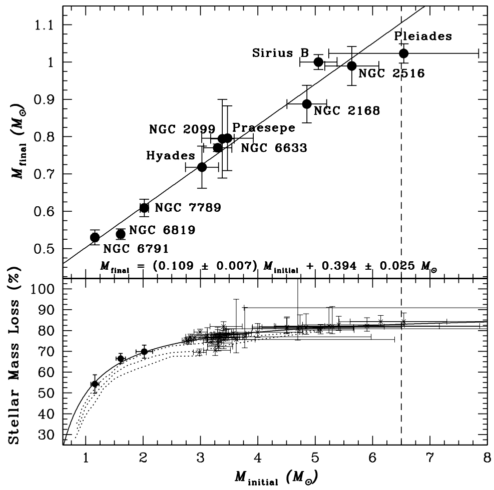

Figure 6.17: *Top*: The relation between the masses of white dwarf progenitors and their final masses from Kalirai et al. (2008), with best linear fit. The entire white dwarf population of a given cluster is represented by a single data point. For the older clusters (e.g., lower initial masses), the white dwarf cooling lifetimes are negligible relative to the age of the cluster, and, therefore, all of the stars at the top of the cooling sequence came from progenitors with the same approximate mass. For the younger clusters, this method averages over small ranges in initial and final mass within each star cluster. The relation shows a roughly linear rise in the remnant mass as a function of the initial mass (see empirical relation on the plot). *Bottom*: The lower panel illustrates the total integrated stellar mass lost through standard evolution, directly constrained from the initial-final mass relation. The individual data points, except at the low mass end, correspond to individual progenitor-white dwarf measurements.

6.11.5 Rare White Dwarf Species and the Physics of Condensed Matter

The temporal coverage of LSST observations in multiple filters will lead to exciting discoveries of exotic stellar species that are astrophysically important. These will include eclipsing short period double degenerate systems, transits of white dwarfs by planetary bodies and other accretion disk objects down to asteroidal dimensions (see also the discussion in § 8.11), and a very large number of pre-cataclysmic variable/post-common envelope systems. The synoptic nature of LSST will be critical in identifying these systems. For some classes, such as eclipses by planets, it may that the LSST cadence will be adequate only for identifying candidates requiring follow-up on smaller telescopes with a much faster cadence.

Eclipsing short period double-degenerate systems are of great interest for several reasons. Follow-up studies of such systems will yield direct determinations of white dwarf radii as well as astrometric masses, which can be used to accurately populate the degenerate mass-radius relation. The catastrophic merger of double degenerate systems is believed to be one potential source of type Ia supernova events. Identifying such systems through their eclipse signals with LSST is a real possibility. Continued monitoring of such systems could reveal the gravitational decay rate of the mutual orbit. It is even conceivable that particular systems found with LSST could be linked to specific gravitational wave signals detected by Laser Interferometer Space Antenna (LISA), since merging white dwarf systems are thought to constitute a major source of the Galactic noise background for LISA.

Some white dwarfs are now known to be orbited by dusty disks and even more show spectral features of heavy elements (Si, Mg, Ca, Fe, and so on), which quickly settle out of the atmosphere indicating on-going accretion. In both cases the source of the dust is believed to be collisions of asteroidal bodies in tight orbits around the white dwarf. Because white dwarfs have small diameters, it is quite possible that favorable orbital plane orientations will reveal transits of substantial bodies from the size of massive Jupiters to asteroids having diameters of tens of km. The gravitational perturbations of such massive bodies are thought to play a role in promoting asteroidal collisions and in maintaining any dusty ring structures that result.

Finally, it should be possible to identify a large number of pre-cataclysmic variable and post-common envelope systems. In general, eclipses (although helpful) are not even necessary since reflection effects produced by the hot white dwarf on the low mass secondary are a frequent signature of these sources. Having a large number of such systems to study will help map out the spectrum of stellar masses and orbital separations that constitute the end states of post-common envelope evolution.

With large numbers of detected white dwarfs, LSST can select those that are variable to the limit of LSST's photometric precision ($\sim 1\%$), and therefore identify new candidate pulsating white dwarfs. Follow-up time-series photometry of these candidates on other telescopes will lead to a substantial number of new white dwarf pulsators, and, therefore, provide a more accurate mapping of the boundaries of the known white dwarf instability strips for pulsation (DAV - H, DBV - He, PG1159 - C) in the HR diagram and in $\log g$ vs $T_{\rm eff}$, and also allow exploration to search for previously unknown instability strips along the white dwarf cooling sequence. A more detailed discussion of LSST's connection to pulsating white dwarfs is provided in § 8.7.2.

LSST will provide a new test for the internal physics of white dwarf stars. The low luminosity end of the white dwarf luminosity functions (WDLF), $\log(L/L_\odot) < -3$, contains information about the equation of state of condensed (degenerate) matter. The shape of the disk WDLF at the turnover (discussed in § 6.11.1) due to the disk's finite age is affected by the release of latent heat of crystallization of the carbon-oxygen white dwarf core. The release of latent heat provides an energy source in an otherwise dead star and slows the white dwarf cooling process. This slowdown manifests itself as an increase in number density of white dwarfs over the luminosity range corresponding to the crystallization event. Even more intriguing is the possibility of having a halo WDLF that is sufficiently populated that we can fully resolve the crystallization bump. LSST's large white dwarf sample will determine if the crystallization bump is indeed present, and if so, at what luminosity (i.e., age), providing new constraints on the equation of state for carbon-oxygen white dwarfs.

6.11.6 The LSST White Dwarf Model Sample

In the following sections we calculate the expected distributions of white dwarfs that LSST will see. The main purpose of these simulations is to estimate the accuracy LSST will obtain in calibrating the white dwarf photometric parallax relation, kinematically separating the disk and halo populations, and measuring their luminosity functions.

In order to generate a simulated sample of disk and halo white dwarfs, five sets of quantities need to be adopted:

1. The expected astrometric and photometric measurement errors.
2. The spatial distribution for each Galaxy component.
3. The distributions of three velocity components.
4. The bolometric luminosity functions.
5. The mapping from bolometric luminosity to broad-band luminosity in each LSST bandpass.

The astrometric and photometric measurement errors are computed as described in Chapter 3. We proceed with detailed descriptions of the remaining quantities.

The Spatial Distribution

LSST will detect white dwarfs to distances much larger than the scale heights and lengths of the Galactic disk. Hence the spatial variation of volume density in the Galaxy must be taken into account. We assume that the spatial distribution of white dwarfs traces the distribution of main sequence stars, both for halo and disk populations (the impact of their different ages is handled through adopted luminosity functions). We ignore bulge white dwarfs in the simulations as they represent only a small fraction of the population. The adopted spatial distribution of main sequence stars, based on recent SDSS-based work by Jurić et al. (2008) is described in § 3.7.1.

The Kinematic Distributions

We assume that the kinematics (distributions of three velocity components) of white dwarfs are the same as the corresponding distribution of main sequence stars, both for halo and disk populations. The adopted kinematic distribution of main sequence stars is based on recent SDSS-based work by Ivezić et al. (2008a).

The White Dwarf Luminosity Function

For disk stars, we adopt the measured luminosity function based on SDSS data (Harris et al. 2006). Using their Figure 4, we obtained the following parameters for a power-law approximation to the measured bolometric Φ (the number of white dwarfs per cubic parsec and magnitude),

$$\begin{aligned} \log\Phi &= -2.65 + 0.26\,(M_{\rm bol} - 15.3) \quad \text{for } 7 < M_{\rm bol} < 15.3 \\ \log\Phi &= -2.65 - 1.70\,(M_{\rm bol} - 15.3) \quad \text{for } 15.3 < M_{\rm bol} < 17.0, \end{aligned} \tag{6.1}$$

which agrees with the data to within 10% at the faint end. The observational knowledge of the halo white dwarf luminosity function is much poorer. Theoretical predictions (Torres et al. 2005, and references therein) indicate an overall shift of the halo luminosity distribution toward fainter absolute magnitudes due to its larger age compared to the disk. Motivated by these predictions and the desire to test the ability to distinguish different luminosity functions when analyzing the simulated sample, we simply shift the Harris et al. (2006) luminosity function by 0.7 mag toward the faint end.

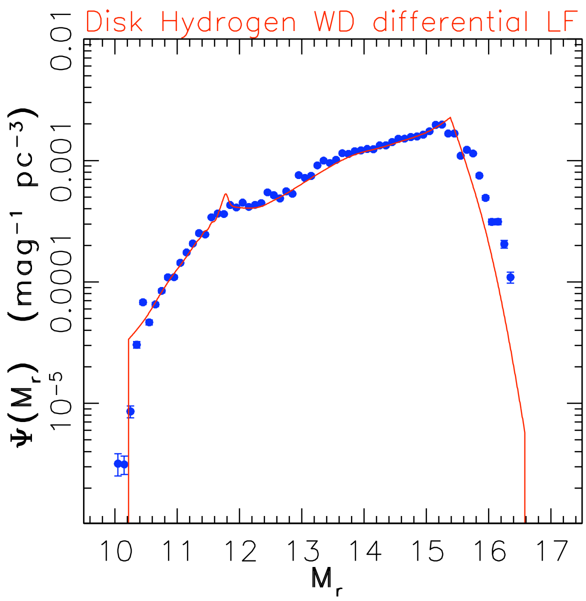

Figure 6.18: Simulated differential luminosity function for candidate hydrogen white dwarfs in the disk sample (normalized to solar neighborhood). The dots with error bars show the result obtained by binning the cumulative luminosity function computed using Lynden-Bell's C^- method in 0.1 mag wide M_r bins (based on $\sim$ 200,000 stars). The red line shows the input luminosity function in the simulation. Note the "feature" in the input luminosity function at $M_r = 11.8$.

We re-express the luminosity function per unit M_r magnitude, Φ_r by multiplying by dM_{bol}/dM_r, determined from the spectral energy distribution, described below. The resulting luminosity functions for disk and halo white dwarfs are shown in Figures 6.18 and 6.19, respectively. The integral of the adopted disk luminosity function is 0.0043 stars pc^{-3} (about 1/10 of the integrated luminosity function for main sequence stars). The disk luminosity function reaches its maximum around $M_r = 15.4$, and the halo luminosity function at $M_r = 16$. Both luminosity functions show a $\sim$ 0.2 mag wide and 20-30% strong "feature" at $M_r \sim 11.8$ which is due to the behavior of dM_{bol}/dM_r.

We assume that 90% of all white dwarfs are hydrogen (DA) white dwarfs and the rest are helium (DB) white dwarfs, but assumed the same luminosity function for both.

The White Dwarf Spectral Energy Distribution

We use models by Bergeron et al. (1995), which produce color tracks that agree with SDSS measurements at the $\sim$0.02 mag level (Eisenstein et al. 2006). Using a sample of $\sim$ 10,000 white dwarfs with SDSS spectroscopic data, Eisenstein et al. (2006) found a very narrow distribution (0.1 dex) of $\log g$ centered on $\log g = 7.9$. Motivated by this result and the desire to simplify analysis of the simulated sample, we adopt a fixed value of $\log g = 8.0$ (Bergeron's models are computed with a $\log g$ step of 0.5 dex). Hence, for a given type of white dwarf atmosphere (hydrogen vs. helium), the models provide unique relationships between M_r and all relevant colors (including bolometric corrections). For hydrogen white dwarfs with $\log g = 8.0$, $M_r = 15.4$ corresponds to an effective

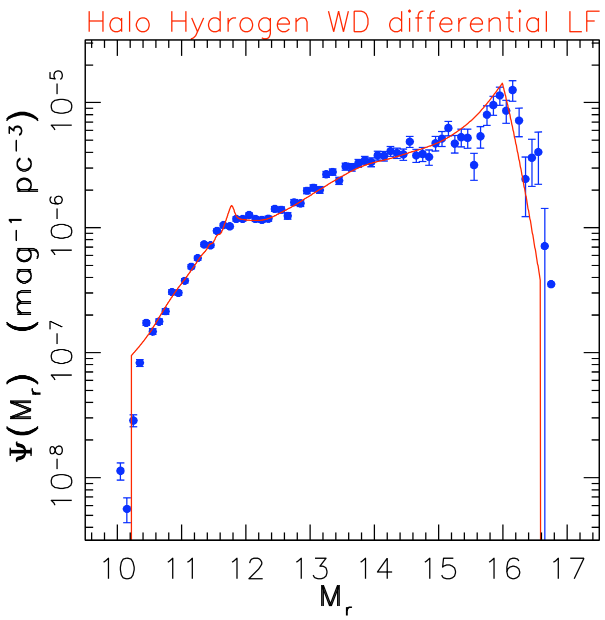

Figure 6.19: Similar to Figure 6.18, now showing the luminosity function for the candidate halo sample.

temperature of 4500 K, mass of 0.58 $M_\odot$ and age of 7.6 Gyr. For $M_r = 16$, the effective temperature is 3900 K, the mass is unchanged and the age is 9.3 Gyr. A 13 Gyr old hydrogen white dwarf, according to Bergeron's models, would have $M_r = 17.4$ and an effective temperature of 2250 K.

Preliminary Analysis of the Simulated White Dwarf Sample

The simulated sample includes $\sim$ 35 million objects with $r < 24.5$ over the whole sky. Here we briefly describe the expected counts of white dwarfs in the main (deep-wide-fast, DWF; see § 2.1) LSST survey, discuss how objects with good trigonometric parallax measurements can be used to derive an empirical photometric parallax relation, and how this relation can be used with proper motion measurements to separate disk and halo candidates. We conclude with preliminary estimates of the accuracy of disk and halo white dwarf luminosity function measurements.

Counts of Simulated White Dwarfs

The main DWF LSST survey is expected to deliver about 1000 visits (summed over all bands) over a $\sim$ 20,000 deg^2 area, and without including the Galactic plane. Figure 6.20 compares cumulative white dwarf counts for several samples. The simulations predict that Gaia's all-sky survey will detect about 240,000 white dwarfs with $r < 20$. Of those, about 1,200 will be halo white dwarfs. These counts are in fair agreement with the results of Torres et al. (2005) who simulated Gaia's performance on white dwarfs. We have also compared the simulated counts to photometrically selected white dwarf candidates from SDSS (see bottom left panel in Fig. 24 of Ivezić et al. 2007). We selected 355 white dwarf candidates over 203 deg^2 defined by $330° < \alpha < 50°$ and $|\delta| < 1.267°$;

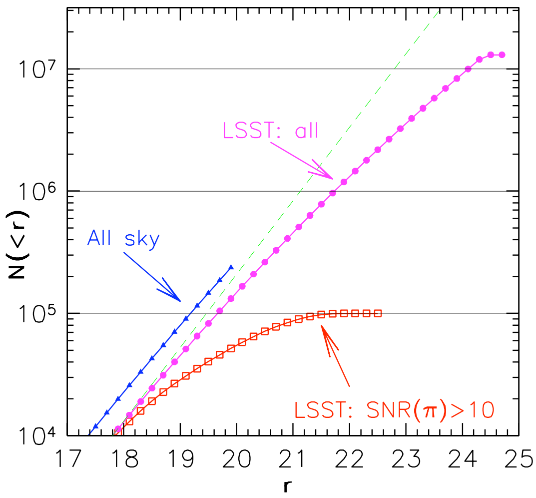

Figure 6.20: A comparison of cumulative white dwarf counts for several samples. The triangles (blue curve) show the counts over the full sky in the magnitude range corresponding to Gaia survey ($r < 20$). The squares (red curve) show the counts of white dwarfs from the main LSST survey (about 1/2 of the sky) that have anticipated signal-to-noise ratio for trigonometric parallax measurements greater than 10. The circles (magenta curve) show the counts of all white dwarfs from the main LSST survey that will have proper motion measurements ($r < 24.5$). The predicted magnitudes are not corrected for the interstellar dust extinction. The dashed line shows the behavior expected for a spatially uniform distribution of sources ($\log[N(< r)] \propto 0.6\,r$) - the impact of Galactic structure is evident in the much shallower slope for simulated counts around $r = 24$.

we required that the objects be non-variable (rms scatter less than 0.07 mag in g) and have $16 < g < 20$, $-0.3 < u - g < 0.5$, $-0.4 < g - r < -0.2$. With the same color-magnitude criteria, the simulated sample includes 340 objects in the same sky region. Given that the observed color-selected sample might include some contamination, this is a robust verification of the model count normalization. The simulations do not include the effects of interstellar extinction, but the extinction over this area is small, and most white dwarfs are close enough to be in front of the majority of the dust.

As illustrated in Figure 6.20, there will be about 13 million white dwarfs with $r < 24.5$ in the DWF survey. While the number of all detected white dwarfs in LSST will be much larger (about 50 million for the $r < 27.5$ limit of co-added data), here we focus only on objects with $r < 24.5$ because they will have, in addition to highly accurate photometry, trigonometric parallax and proper motion measurements. In particular, about 375,000 simulated objects have anticipated signal-to-noise ratio for trigonometric parallax measurements greater than 5 and 104,000 greater than 10. This latter subsample (whose cumulative counts are shown in Figure 6.20) can be used to empirically constrain photometric parallax relations for hydrogen and helium white dwarfs and to train color-based classification algorithms, as described next. In the remainder of this analysis, we assume no knowledge of the input model parameters except when estimating the performance parameters such as sample completeness and contamination.

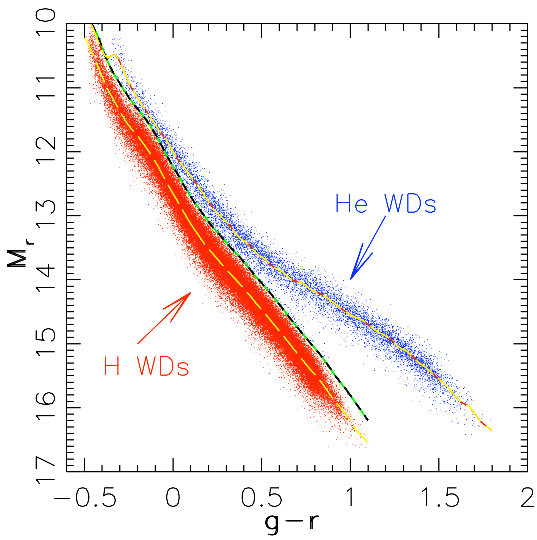

Figure 6.21: The calibration of the photometric parallax relation, $M_r(g-r)$, for white dwarfs. The M_r values are based on trigonometric parallax and "measured" r band magnitudes. The dots represent $\sim$ 100,000 simulated objects with the signal-to-noise ratio for trigonometric parallax measurements greater than 10. The middle dashed line is the color-magnitude separator described in the text. The other two lines are the median M_r vs. $g-r$ photometric parallax sequences. The true relations used to generate the simulated sample are indistinguishable (rms $\sim$ 0.01 mag) from these empirically determined median values.

White Dwarf Photometric Parallax Relations

The distribution of the difference between trigonometric and true distance moduli for the 104,000 white dwarfs with parallax S/N$>$ 10 is close to Gaussian, with a median value of -0.03 mag and an rms scatter of 0.15 mag. For the subset of 10,000 objects with $r < 18$, the rms scatter is 0.10 mag and the bias is below 0.01 mag.

The absolute magnitude based on "measured" trigonometric parallax as a function of "measured" $g-r$ color is shown in Figure 6.21. The two sequences that correspond to hydrogen and helium white dwarfs are easily discernible. A simple separator of hydrogen and helium color-magnitude sequences is obtained by shifting the median M_r vs. $g-r$ curve for hydrogen white dwarfs by 0.4 mag towards the bright end. A slightly better choice would be to account for the shape of the helium sequence as well. The application of this separator results in correct classification for 99.6% of the objects in the candidate hydrogen sample and for 96.3% of the objects in the candidate helium sample.

Photometric Separation of Hydrogen and Helium White Dwarfs

The separation of hydrogen and helium white dwarfs based on the M_r vs. $g-r$ diagram is possible only for objects with high S/N trigonometric parallax measurements. Since such objects represent only about 1% of the full $r < 24.5$ LSST white dwarf sample, a color separation method is required to classify the latter sample. Although helium white dwarfs represent only 10% of all objects, the

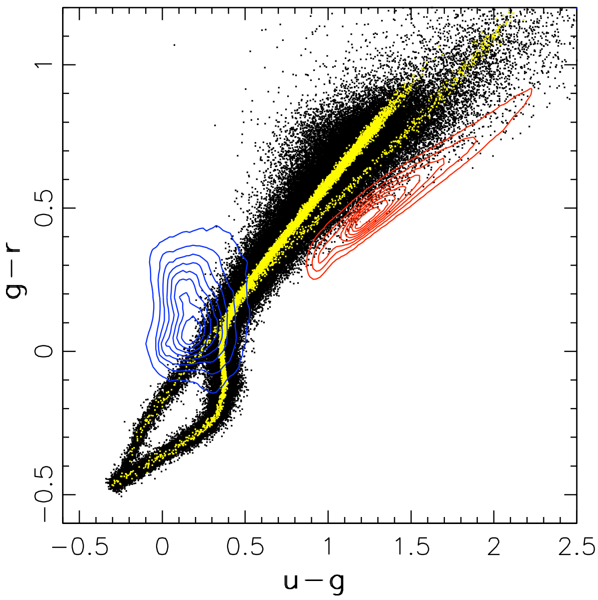

Figure 6.22: The distribution of the simulated white dwarfs in the $g-r$ vs. $u-g$ color-color diagram. Black points show objects with $r < 24.5$ and $b > 60°$. Yellow points show a subsample of predominantly brighter sources that have 10σ or better "measurement" of the trigonometric parallax. The two sequences correspond to He and H white dwarfs. The distribution of low-redshift ($z < 2.2$) quasars observed by SDSS is shown by blue contours. The blue part of the stellar locus (dominated by F and G stars), as observed by SDSS, is shown by the red contours. LSST photometry will be sufficiently accurate not only to separate white dwarfs from quasars and main sequence stars, but also to separate hydrogen from helium white dwarfs (the sequences do not overlap in the multi-dimensional color space, see text).

differences in M_r vs. $g-r$ relations between helium and hydrogen white dwarfs might significantly bias the luminosity function determination.

We use the two candidate samples with good trigonometric parallax measurements to quantify their multi-dimensional color tracks. Figure 6.22 shows the two-dimensional projection of these tracks. At the hot end, the tracks for hydrogen and helium objects are well separated. Although they appear to cross around $g-r = 0.2$, they are still separated in the four-dimensional color space spanned by the $u-g$, $g-r$, $r-i$ and $i-z$ colors[3].

For each sample, we compute the median $u-g$, $r-i$ and $i-z$ color for each 0.01 mag wide bin of $g-r$ color. Using these tracks, for each star we compute the shortest distance to each locus, denoted here D_{He} and D_H. The difference between these two four-dimensional color distances (4DCD) can be used as a simple color-based classifier. For the training sample, which has small photometric errors due to the relatively bright flux limit imposed by requiring high trigonometric parallax signal-to-noise ratio, the separation is essentially perfect (mis-classification rate, or sample contamination, is less than 1%).

We assess the performance of color separation at the faint end by resorting to true input class, and study the completeness and contamination of candidate samples as a function of $\delta_{4DCD} =$

[3]Reliable colors are not yet available for the y band so we do not consider it here.

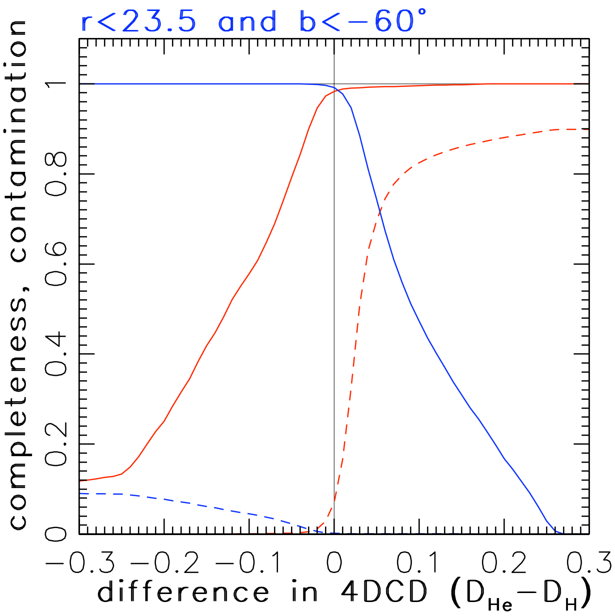

Figure 6.23: The completeness and contamination for color-selected subsamples of hydrogen and helium white dwarfs, as a function of the difference between distances to each four-dimensional color sequence ($\delta_{4DCD} = D_{He} - D_H$). The solid lines show completeness and dashed lines show contamination. The blue lines correspond to hydrogen subsample, and red lines to helium subsample. Objects are classified as helium white dwarfs if their δ_{4DCD} is smaller than the adopted cut-off value. The panel shows a flux-limited sample with $r < 23.5$.

$D_{He} - D_H$ (see Figure 6.23). The optimal value of δ_{4DCD} for separating two object types is a trade-off and depends on whether a particular science case requires high completeness or low contamination. Typically the best δ_{4DCD} value is not zero because hydrogen white dwarfs are ten times as numerous as helium white dwarfs. These effects can be elegantly treated using the Bayesian formalism developed by Mortlock et al. (2008), hereafter MPI08. Here we follow a simpler approach and, informed by the results shown in Figure 6.23, adopt $\delta_{4DCD} = -0.05$ for the rest of the analysis presented here. For $r < 23.5$, the candidate helium sample completeness and contamination are 79% and 0.2%, respectively (see the right panel in Figure 6.23). Where $r < 24.5$, the completeness of 99% with a contamination of 3% for the candidate hydrogen sample, and 73% and 14%, respectively, for the candidate helium sample, the degraded but still remarkable performance being attributed to larger photometric errors.

We note that despite high completeness for the helium subsample, there are ranges of M_r, such as $M_r \sim 12.5$, where it is sufficiently small to induce large systematic errors in luminosity function. To properly treat the helium subsample, a more sophisticated method, such as that described by MPI08, is required. Nevertheless, the simplistic δ_{4DCD} method used here produces sufficiently clean samples of candidate hydrogen white dwarfs for further analysis.

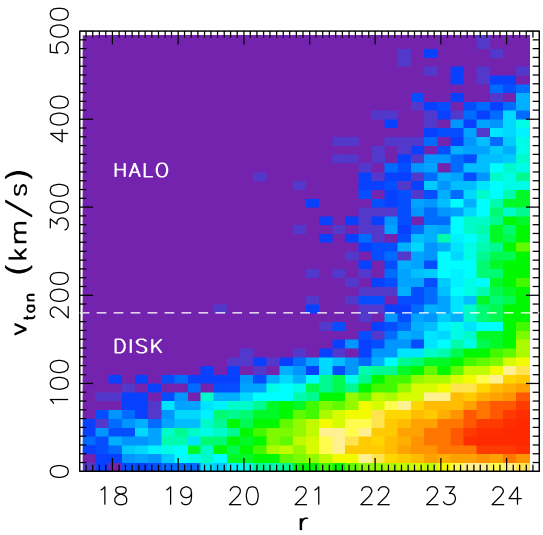

Figure 6.24: The dependence of tangential velocity on apparent magnitude for white dwarfs with $b > 60°$. The map shows counts of stars in each bin on logarithmic scale, increasing from blue to red. The tangential velocity is computed from each star's measured proper motion and distance estimate from the photometric parallax relation shown in Figure 6.21. At faint magnitudes ($r > 22$), the sample contains a large fraction of halo white dwarfs. The horizontal line at 180 km s^{-1} separates disk and halo stars with sample completeness and contamination of 99% and 3%, respectively, for disk stars, and 78% and 6%, respectively, for halo stars.

Kinematic Separation of Disk and Halo White Dwarfs

The measured proper motion and distance estimate can be used to probabilistically assign disk or halo membership, if suitable kinematic models exist, for an arbitrary direction on the sky. In the general case, the observed proper motion depends on a linear combination of all three velocity components, and the probabilistic class assignment can be computed following the approach outlined in MPI08 (the standard method for separating disk and halo stars based on reduced proper motion diagram will fail at kpc distances probed by LSST, see Appendix B in Sesar et al. 2008). In this preliminary analysis, we limit our sample to the region with $b < -60°$, where proper motion primarily depends on radial, v_R, and azimuthal (rotational), v_ϕ, components, while the vertical velocity component, v_Z, is by and large absorbed into the radial (along the line of sight) velocity component.

From $\sim$ 273,000 simulated objects with $r < 24.5$ and $b < -60°$ (2,680 deg^2), we select $\sim$ 250,000 candidate hydrogen white dwarfs using the color-based classification described above. We determine their distances using a photometric parallax relation, and compute the absolute value of their tangential velocity, v_{tan}. The distribution of v_{tan} as a function of measured apparent r band magnitude for this sample is shown in Figure 6.24. The median difference between the "measured" and true v_{tan} is 3 km s^{-1}, and ranges from 1 km s^{-1} at distances smaller than 400 pc, to 30 km s^{-1} at a distance of 5 kpc.

The v_{tan} distribution is clearly bimodal, with high v_{tan} stars corresponding to the halo sample. Notably a significant fraction of halo white dwarfs is seen only at $r > 22$. Just as in the case of color separation of the hydrogen and helium sequences, the optimal separation of disk and halo

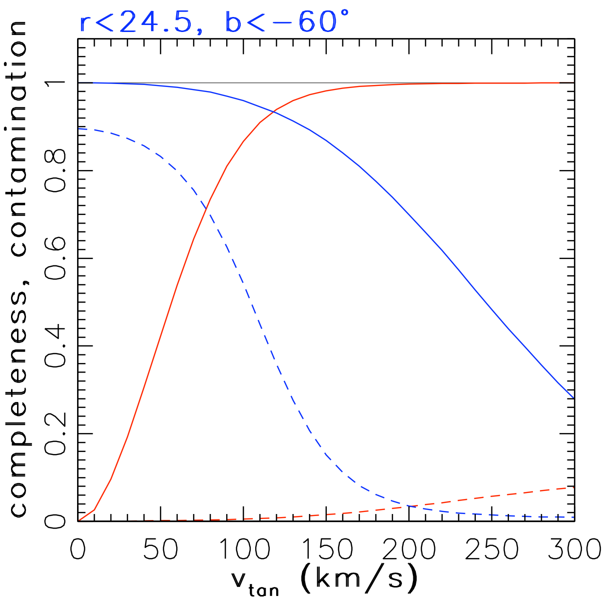

Figure 6.25: The completeness and contamination of candidate disk and halo subsamples selected by tangential velocity. The solid lines show completeness and dashed lines show contamination. The blue lines correspond to halo subsample, and red lines to disk subsample. Objects are classified as disk candidates if their tangential velocity is smaller than the adopted cut-off value.

candidates by v_{tan} includes a trade-off between completeness and contamination, as illustrated in Figure 6.25.

Informed by Figure 6.25, we select $\sim$ 195,000 candidate disk members by requiring $v_{tan} < 100$ km s^{-1}, and $\sim$ 19,000 candidate halo members by requiring $v_{tan} > 200$ km s^{-1}. These samples are optimized for low contamination: the sample contamination for halo candidates is 3.5% and 0.5% for disk candidates. The sample completeness is 70% for the halo sample and 87% for the disk sample. We proceed to determine the luminosity function for these two samples.

Determination of Disk and Halo White Dwarf Luminosity Functions

There are many different methods for estimating a luminosity function from data (e.g., Kelly et al. 2008, and references therein). In the case of uncorrelated variables (the luminosity function is independent of position once disk and halo candidates are separated. With real data this assumption can be tested, e.g., Fan et al. 2001). One of the best methods is the C^- method (Lynden-Bell 1971), because it requires binning in only one coordinate. We used the C^- method to determine the luminosity functions shown in Figures 6.18 and 6.19.

Although the sample analyzed here ($b < -60°$) includes only about 10% of the total DWF area (and $\sim$2% of the white dwarf counts for the entire LSST sample), the random (statistical) errors for both disk and halo luminosity functions are negligible. The dominant systematic errors (with an rms scatter of about 10%) are due to errors in the photometric parallax relation: when the true M_r values are used, the C^- method reproduces the input luminosity function essentially perfectly.

This nearly perfect agreement also demonstrates that the hydrogen vs. helium separation, and disk vs. halo separation algorithms have satisfactory performance. Most importantly, the faint end of the luminosity functions for both disk and halo samples is correctly reproduced to within 0.1-0.2 mag.

6.12 A Comparison of Gaia and LSST Surveys

Laurent Eyer, Željko Ivezić, David Monet

In this section, we compare the design predictions for the astrometric and photometric performance of the Gaia mission and the LSST system. For Gaia's performance, we have collected and parametrized predictions from various technical documents, and discussed the adopted model with Gaia key technical personnel. For LSST performance, we adopted parameters listed in Chapter 1. While the various adopted errors are probably accurate to much better than a factor of two for both Gaia and LSST, their ultimate values cannot be more precisely known before their data products are delivered.

6.12.1 Photometric Errors

To determine photometric errors for Gaia and LSST, we follow the discussion in § 3.5. For Gaia, we adopt $\sigma_{sys} = 0.001$ mag and $\sigma_{sys} = 0.0005$ mag for single transit and the end-of-mission values in the G band, respectively. For LSST, we adopt $\sigma_{sys} = 0.003$ mag. We model random photometric errors (per transit) for Gaia as

$$\sigma_{rand} = 0.02 \times 10^{0.2(G-20)} \ \ \text{(mag)}, \tag{6.2}$$

where G is the Gaia's broad-band magnitude[4]. We described the model for LSST's photometric errors in Equation 3.2.

The behavior of photometric errors as a function of r band magnitude for Gaia, LSST and SDSS is illustrated in the top panel in Figure 6.26 (for SDSS, we used Equation 3.2 and $m_5 = 22.1$ in the r band).

6.12.2 Trigonometric Parallax and Proper Motion Errors

Similarly to our treatment of photometric errors, we add systematic and random astrometric errors in quadrature(see Equation 3.1). For Gaia, we set a systematic trigonometric parallax error of 0.007 mas, and model the random errors as

$$\sigma^{\pi}_{rand} = 0.30 \times 10^{0.22(G-20)} \ \ \text{(mas)}. \tag{6.3}$$

[4]More elaborate models have been produced, for example by C. Jordi; however, for our purpose this simplified model is a sufficiently accurate approximation.

We obtain proper motion errors (per coordinate) by multiplying trigonometric parallax errors by 0.66 yr^{-1}. We compute LSST trigonometric parallax and proper motion errors using identical expressions with performance parameters listed in Table 3.3.

The behavior of trigonometric parallax and proper motion errors as function of r band magnitude for Gaia and LSST is illustrated in the bottom two panels in Figure 6.26. For comparison, we also show proper motion error behavior for the current state-of-the-art large-area database constructed by Munn et al. (2004) using SDSS and Palomar Observatory Sky Survey data (a baseline of 50 years). Following Bond et al. (2009), the SDSS-POSS proper motion errors (per coordinate) are modeled as

$$\sigma^{\mu}_{\mathrm{SDSS-POSS}} = 2.7 + 2.0 \times 10^{0.4(r-20)} \ \ (\mathrm{mas/yr}). \tag{6.4}$$

(Compare with Table 3.3 to see how much better LSST will do.) All adopted performance parameters for LSST and Gaia are summarized in Table 6.6.

6.12.3 Implications for Science Projects

Gaia will provide an all-sky map with exquisite trigonometric parallax, proper motion and photometric measurements to $r \sim 20$ for about billion stars. LSST will extend this map to $r \sim 27$ over half of the sky, and detect about 10 billion stars. Due to Gaia's superb astrometric and photometric measurements, and LSST's significantly deeper data, the two surveys are highly complementary: Gaia will map the Milky Way's disk with unprecedented detail, and LSST will extend this map all the way to the halo edge.

For example, stars just below the main sequence turn-off with $M_r = 4.5$ will be detected by Gaia to a distance limit of ∼10 kpc ($r < 20$), and to ∼100 kpc with LSST's single-epoch data ($r < 24.5$). Ivezić et al. (2008b) estimated that LSST will obtain metallicity measurements accurate to 0.2 dex or better, with proper motion measurements accurate to ∼0.2 mas/yr or better, for about 200 million F/G dwarf stars within 100 kpc. For intrinsically faint stars, such as late M dwarfs, L/T dwarfs, and white dwarfs, the deeper limit of LSST will enable detection and characterization of halo populations. A star with $M_r = 15$ will be detectable to a distance limit of 100 pc with Gaia and ∼800 pc with LSST, and hence LSST samples will be about 100 times larger. For a substantial fraction of red stars with $r > 20$, LSST will provide trigonometric parallax measurements accurate to better than 10% (see Figure 3.13). In summary, LSST will represent a deep complement to Gaia.

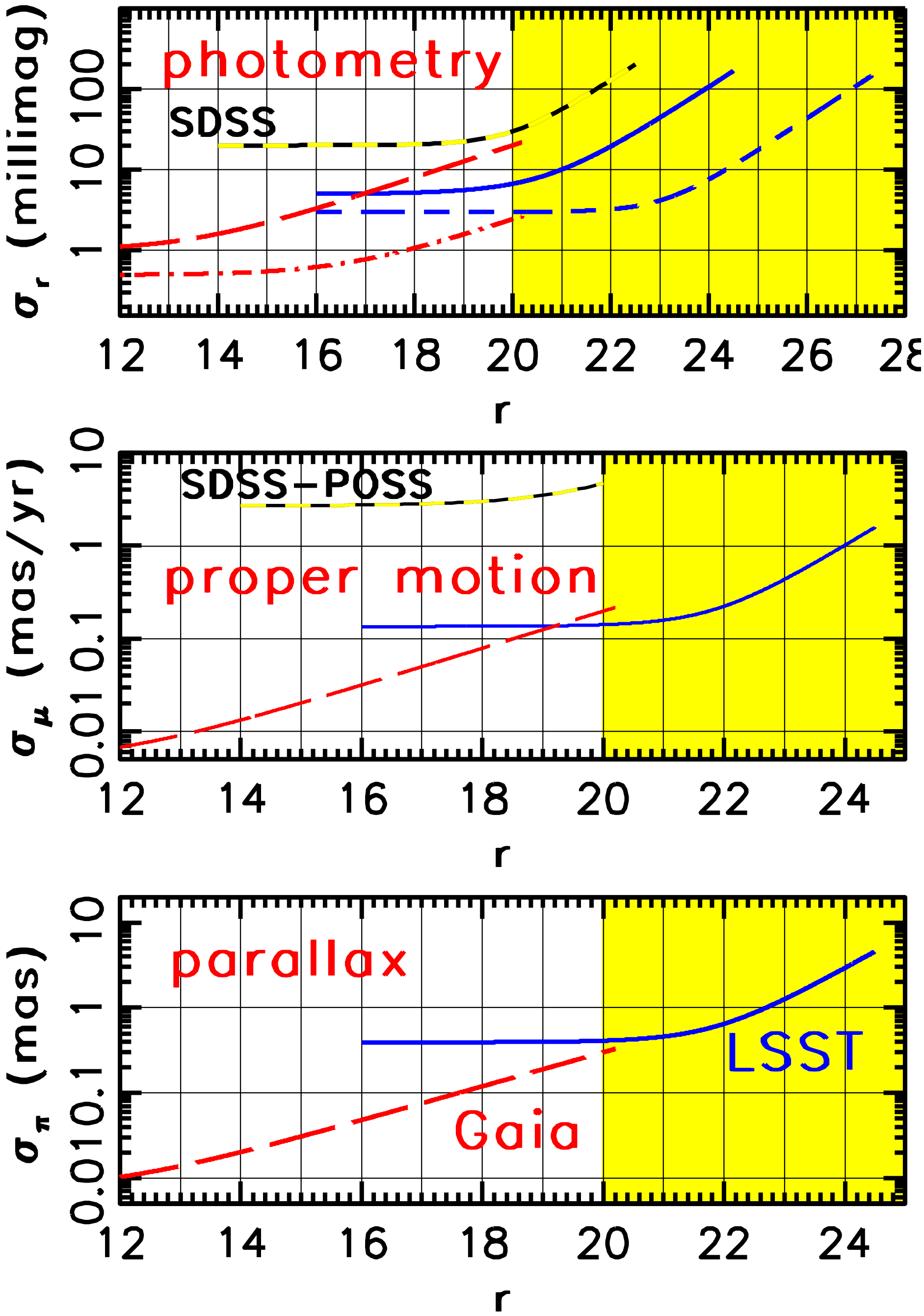

Figure 6.26: A comparison of photometric, proper motion and parallax errors for SDSS, Gaia and LSST, as a function of apparent magnitude r, for a G2V star (we assumed $r = G$, where G is the Gaia's broad-band magnitude). In the top panel, the curve marked "SDSS" corresponds to a single SDSS observation. The red curves correspond to Gaia; the long-dashed curve shows a single *transit* accuracy, and the dot-dashed curve the end of mission accuracy (assuming 70 transits). The blue curves correspond to LSST; the solid curve shows a single *visit* accuracy, and the short-dashed curve shows accuracy for co-added data (assuming 230 visits in the r band). The curve marked "SDSS-POSS" in the middle panel shows accuracy delivered by the proper motion catalog of Munn et al. (2004). In the middle and bottom panels, the long-dashed curves correspond to Gaia, and the solid curves to LSST. Note that LSST will smoothly extend Gaia's error vs. magnitude curves four magnitudes fainter. The assumptions used in these computations are described in the text.

Table 6.6: Adopted Gaia and LSST Performance

Quantity	Gaia	LSST
Sky Coverage	whole sky	half sky
Mean number of epochs	70 over 5 yrs	1000 over 10 yrs
Mean number of observations	320[a] over 5 yrs	1000[b] over 10 yrs
Wavelength Coverage	320–1050 nm	*ugrizy*
Depth per visit (5σ, r band)	20	24.5; 27.5[c]
Bright limit (r band)	6	16-17
Point Spread Function (arcsec)	0.14×0.4	0.70 FWHM
Pixel count (Gigapix)	1.0	3.2
Syst. Photometric Err. (mag)	0.001, 0.0005[d]	0.005, 0.003[e]
Syst. Parallax Err. (mas)	0.007[f]	0.40[f]
Syst. Prop. Mot. Err. (mas/yr)	0.004	0.14

[a] One transit includes the G-band photometry (data collected over 9 CCDs), BP and RP spectrophotometry, and measurements by the SkyMapper and RVS instruments.
[b] Summed over all six bands (taken at different times).
[c] For co-added data, assuming 230 visits.
[d] Single transit and the end-of-mission values for the G band (from SkyMapper; integrated BP and RP photometry will be more than about 3 times less precise).
[e] For single visit and co-added observations, respectively.
[f] Astrometric errors depend on source color. The listed values correspond to a G2V star.

References

Alcock, C. et al., 1995, *AJ*, 109, 1653
—, 2000, *ApJ*, 542, 281
Barnes, S. A., 2003, *ApJ*, 586, 464
Barry, D. C., 1988, *ApJ*, 334, 436
Beers, T. C., & Christlieb, N., 2005, *ARAA*, 43, 531
Beers, T. C., Lee, Y. S., Peruta, C., Sivarani, T., Allende Prieto, C., Aoki, W., Carollo, D., & SDSS, 2009, American Astronomical Society Meeting Abstracts, Vol. 213, The Lowest Metallicity Stars from SDSS/SEGUE. p. 416
Belokurov, V. et al., 2006, *ApJL*, 642, L137
Berger, E. et al., 2001, *Nature*, 410, 338
Bergeron, P., Liebert, J., & Fulbright, M. S., 1995, *ApJ*, 444, 810
Besla, G., Kallivayalil, N., Hernquist, L., van der Marel, R. P., Cox, T. J., Robertson, B., & Alcock, C., 2009, in IAU Symposium, Vol. 256, The binarity of the Clouds and the formation of the Magellanic Stream, pp. 99–104
Binney, J., 2001, in Astronomical Society of the Pacific Conference Series, Vol. 240, Gas and Galaxy Evolution, J. E. Hibbard, M. Rupen, & J. H. van Gorkom, eds., p. 355
Bochanski, J. J., West, A. A., Hawley, S. L., & Covey, K. R., 2007, *AJ*, 133, 531
Boeshaar, P. C., Margoniner, V., & The Deep Lens Survey Team, 2003, in IAU Symposium, Vol. 211, Brown Dwarfs, E. Martín, ed., p. 203
Bond, N. A., Ivezic, Z., Sesar, B., Juric, M., & Munn, J., 2009, ArXiv e-prints, 0909.0013
Bouy, H., Brandner, W., Martín, E. L., Delfosse, X., Allard, F., & Basri, G., 2003, *AJ*, 126, 1526
Bruzual, G., & Charlot, S., 2003, *MNRAS*, 344, 1000
Burgasser, A. J. et al., 2003a, *ApJ*, 592, 1186
Burgasser, A. J., Kirkpatrick, J. D., Liebert, J., & Burrows, A., 2003b, *ApJ*, 594, 510
Burgasser, A. J., Lepine, S., Lodieu, N., Scholz, R. D., Delorme, P., Jao, W. C., Swift, B. J., & Cushing, M. C., 2008, Proc. of the 15th Cambridge Workshop on Cool Stars, Stellar Systems, and the Sun, in prep., arXiv:astro-ph/0810.0569
Burgasser, A. J., Liebert, J., Kirkpatrick, J. D., & Gizis, J. E., 2002, *AJ*, 123, 2744
Burgasser, A. J., Reid, I. N., Siegler, N., Close, L., Allen, P., Lowrance, P., & Gizis, J., 2007, in Protostars and Planets V, B. Reipurth, D. Jewitt, & K. Keil, eds., pp. 427–441
Burrows, A., Hubbard, W. B., Saumon, D., & Lunine, J. I., 1993, *ApJ*, 406, 158
Burrows, A., Sudarsky, D., & Hubeny, I., 2006, *ApJ*, 640, 1063
Burrows, A., Sudarsky, D., & Lunine, J. I., 2003, *ApJ*, 596, 587
Carollo, D. et al., 2007, *Nature*, 450, 1020
Catelan, M., Stephens, A. W., & Contreras, R. P., 2005, American Astronomical Society Meeting Abstracts, 207, 128.11
Caulet, A., Gruendl, R. A., & Chu, Y.-H., 2008, *ApJ*, 678, 200
Chaboyer, B., 2000, in Liege International Astrophysical Colloquia, Vol. 35, Liege International Astrophysical Colloquia, A. Noels, P. Magain, D. Caro, E. Jehin, G. Parmentier, & A. A. Thoul, eds., p. 451
Chen, C.-H. R., Chu, Y.-H., Gruendl, R. A., Gordon, K. D., & Heitsch, F., 2009, *ApJ*, 695, 511
Cignoni, M., Degl'Innocenti, S., Prada Moroni, P. G., & Shore, S. N., 2006, *A&A*, 459, 783
Clement, C. M. et al., 2001, *AJ*, 122, 2587
Coleman, G. D., Wu, C.-C., & Weedman, D. W., 1980, *ApJS*, 43, 393
Cruz, K. L. et al., 2007, *AJ*, 133, 439
Cushing, M. C., Looper, D., Burgasser, A. J., Kirkpatrick, J. D., Faherty, J., Cruz, K. L., Sweet, A., & Sanderson, R. E., 2009, *ApJ*, 696, 986
Cushing, M. C., Rayner, J. T., & Vacca, W. D., 2005, *ApJ*, 623, 1115
D'Antona, F., 2002, in IAU Symposium, Vol. 207, Extragalactic Star Clusters, D. P. Geisler, E. K. Grebel, & D. Minniti, eds., p. 599
de la Fuente Marcos, R., & de la Fuente Marcos, C., 2004, *New Astronomy*, 9, 475
DeGennaro, S. et al., 2009, in prep.
Demory, B. et al., 2009, ArXiv e-prints, 0906.0602
Digby, A. P., Hambly, N. C., Cooke, J. A., Reid, I. N., & Cannon, R. D., 2003, *MNRAS*, 344, 583
Dohm-Palmer, R. C., Skillman, E. D., Mateo, M., Saha, A., Dolphin, A., Tolstoy, E., Gallagher, J. S., & Cole, A. A., 2002, *AJ*, 123, 813

Dolphin, A. E., 2002a, in Astronomical Society of the Pacific Conference Series, Vol. 274, Observed HR Diagrams and Stellar Evolution, T. Lejeune & J. Fernandes, eds., p. 503
—, 2002b, *MNRAS*, 332, 91
Duquennoy, A., & Mayor, M., 1991, *A&A*, 248, 485
Eisenstein, D. J. et al., 2006, *ApJS*, 167, 40
Fan, X. et al., 2001, *AJ*, 121, 54
Fischer, D. A., & Marcy, G. W., 1992, *ApJ*, 396, 178
Freeman, K., & Bland-Hawthorn, J., 2002, *ARAA*, 40, 487
Fuchs, B., Jahreiß, H., & Flynn, C., 2009, *AJ*, 137, 266
Fukui, Y. et al., 2008, *ApJS*, 178, 56
Girardi, L., Bertelli, G., Bressan, A., Chiosi, C., Groenewegen, M. A. T., Marigo, P., Salasnich, B., & Weiss, A., 2002, *A&A*, 391, 195
Girardi, L., Bressan, A., Bertelli, G., & Chiosi, C., 2000, *A&A*, 141, 371
Gizis, J. E., Monet, D. G., Reid, I. N., Kirkpatrick, J. D., Liebert, J., & Williams, R. J., 2000, *AJ*, 120, 1085
Gizis, J. E., Reid, I. N., & Hawley, S. L., 2002, *AJ*, 123, 3356
Gouliermis, D., Brandner, W., & Henning, T., 2006a, *ApJ*, 641, 838
—, 2006b, *ApJL*, 636, L133
Gouliermis, D. A., Henning, T., Brandner, W., Dolphin, A. E., Rosa, M., & Brandl, B., 2007, *ApJL*, 665, L27
Grether, D., & Lineweaver, C. H., 2006, *ApJ*, 640, 1051
Grillmair, C. J., 2006, *ApJL*, 645, L37
Gruendl, R. A., & Chu, Y.-H., 2009, ArXiv e-prints, 0908.0347
Habing, H. J., 1996, *A&AS*, 7, 97
Hall, P. B., 2002, *ApJL*, 580, L77
Hansen, B. M. S. et al., 2007, *ApJ*, 671, 380
—, 2002, *ApJL*, 574, L155
Harris, H. C. et al., 2006, *AJ*, 131, 571
Hartman, J. D. et al., 2009, *ApJ*, 691, 342
Hawley, S. L., Reid, I. N., & Tourtellot, J. G., 2000, in Very Low-mass Stars and Brown Dwarfs, Cambridge University Press, UK, R. Rebolo & M. R. Zapatero-Osorio, eds., p. 109
Helmi, A., & White, S. D. M., 1999, *MNRAS*, 307, 495
Hertzsprung, E., 1905, *Zeitschrift fur Wissenschaftliche Photographie*, 3, 442
Hewett, P. C., Warren, S. J., Leggett, S. K., & Hodgkin, S. T., 2006, *MNRAS*, 367, 454
Horne, J. H., & Baliunas, S. L., 1986, *ApJ*, 302, 757
Hurley, J. R. et al., 2008, *AJ*, 135, 2129
Ibata, R. A., Gilmore, G., & Irwin, M. J., 1994, *Nature*, 370, 194
Ivezić, Ž. et al., 2008a, *ApJ*, 684, 287
—, 2007, *AJ*, 134, 973
—, 2008b, ArXiv e-prints, 0805.2366
Jurić, M. et al., 2008, *ApJ*, 673, 864
Kalirai, J. S., Bergeron, P., Hansen, B. M. S., Kelson, D. D., Reitzel, D. B., Rich, R. M., & Richer, H. B., 2007, *ApJ*, 671, 748
Kalirai, J. S., Hansen, B. M. S., Kelson, D. D., Reitzel, D. B., Rich, R. M., & Richer, H. B., 2008, *ApJ*, 676, 594
Kalirai, J. S. et al., 2001a, *AJ*, 122, 257
Kalirai, J. S., & Tosi, M., 2004, *MNRAS*, 351, 649
Kalirai, J. S., Ventura, P., Richer, H. B., Fahlman, G. G., Durrell, P. R., D'Antona, F., & Marconi, G., 2001b, *AJ*, 122, 3239
Kallivayalil, N., van der Marel, R. P., & Alcock, C., 2006a, *ApJ*, 652, 1213
Kallivayalil, N., van der Marel, R. P., Alcock, C., Axelrod, T., Cook, K. H., Drake, A. J., & Geha, M., 2006b, *ApJ*, 638, 772
Kanbur, S. M., & Fernando, I., 2005, *MNRAS*, 359, L15
Keller, S. C. et al., 2007, Publications of the Astronomical Society of Australia, 24, 1
Kelly, B. C., Fan, X., & Vestergaard, M., 2008, *ApJ*, 682, 874
Kennicutt, Jr., R. C., & Hodge, P. W., 1986, *ApJ*, 306, 130
Kim, S., Staveley-Smith, L., Dopita, M. A., Sault, R. J., Freeman, K. C., Lee, Y., & Chu, Y.-H., 2003, *ApJS*, 148, 473
Kinman, T. D., 1959, *MNRAS*, 119, 559

Kirkpatrick, J. D., 2005, *ARAA*, 43, 195
Kirkpatrick, J. D. et al., 1999, *ApJ*, 519, 802
Kraus, A. L., & Hillenbrand, L. A., 2007, *AJ*, 134, 2340
Krauss, L. M., & Chaboyer, B., 2003, *Science*, 299, 65
Lada, C. J., & Lada, E. A., 2003, *ARAA*, 41, 57
Lee, J.-W., & Carney, B. W., 1999, *AJ*, 118, 1373
Lee, Y.-W., Demarque, P., & Zinn, R., 1990, *ApJ*, 350, 155
Leggett, S. K., Ruiz, M. T., & Bergeron, P., 1998, *ApJ*, 497, 294
Liebert, J., Kirkpatrick, J. D., Cruz, K. L., Reid, I. N., Burgasser, A., Tinney, C. G., & Gizis, J. E., 2003, *AJ*, 125, 343
Loebman, S. et al., 2008, in American Institute of Physics Conference Series, Vol. 1082, SDSS Observations of the Milky Way vs. N-body Models: A Comparison of Stellar Distributions in the Position-Velocity-Metallicity Space, pp. 238–242
López-Morales, M., 2007, *ApJ*, 660, 732
Lynden-Bell, D., 1971, *MNRAS*, 155, 95
Mainzer, A. K., Eisenhardt, P., Wright, E. L., Liu, F.-C., Irace, W., Heinrichsen, I., Cutri, R., & Duval, V., 2005, in Society of Photo-Optical Instrumentation Engineers (SPIE) Conference Series, Vol. 5899, Preliminary design of the Wide-Field Infrared Survey Explorer (WISE), H. A. MacEwen, ed., pp. 262–273
Mamajek, E. E., & Hillenbrand, L. A., 2008, ArXiv e-prints, 0807.1686
Marigo, P., Girardi, L., Bressan, A., Groenewegen, M. A. T., Silva, L., & Granato, G. L., 2008, *A&A*, 482, 883
Martín, E. L., Barrado y Navascués, D., Baraffe, I., Bouy, H., & Dahm, S., 2003, *ApJ*, 594, 525
Massey, P., Lang, C. C., Degioia-Eastwood, K., & Garmany, C. D., 1995, *ApJ*, 438, 188
Mathieu, R. D., 2000, in Astronomical Society of the Pacific Conference Series, Vol. 198, Stellar Clusters and Associations: Convection, Rotation, and Dynamos, R. Pallavicini, G. Micela, & S. Sciortino, eds., p. 517
Meibom, S., 2008, ArXiv e-prints, 0812.5078
Meibom, S., Mathieu, R. D., & Stassun, K. G., 2008, ArXiv e-prints, 0805.1040
Metchev, S. A., & Hillenbrand, L., 2007, in Bulletin of the American Astronomical Society, Vol. 38, The Mass Function of Brown Dwarf and Stellar Companions, p. 781
Mortlock, D. J., Peiris, H. V., & Ivezić, Ž., 2008, ArXiv e-prints, 0810.5123
Munn, J. A. et al., 2004, *AJ*, 127, 3034
Odenkirchen, M. et al., 2001, *ApJL*, 548, L165
Oosterhoff, P. T., 1939, *The Observatory*, 62, 104
Oswalt, T. D., Smith, J. A., Wood, M. A., & Hintzen, P., 1996, *Nature*, 382, 692
Ott, J. et al., 2008, Publications of the Astronomical Society of Australia, 25, 129
Patten, B. M. et al., 2006, *ApJ*, 651, 502
Piatek, S., Pryor, C., & Olszewski, E. W., 2008, *AJ*, 135, 1024
Pickles, A. J., 1998, *PASP*, 110, 863
Prša, A., Guinan, E. F., Devinney, E. J., DeGeorge, M., Bradstreet, D. H., Giammarco, J. M., Alcock, C. R., & Engle, S. G., 2008, *ApJ*, 687, 542
Prša, A., Pepper, J., & Stassun, K., 2009, *PASP*, in preparation
Prša, A., & Zwitter, T., 2005, *ApJ*, 628, 426
Reid, I. N., Turner, E. L., Turnbull, M. C., Mountain, M., & Valenti, J. A., 2007, *ApJ*, 665, 767
Reiners, A., & Basri, G., 2006, *AJ*, 131, 1806
—, 2008, *ApJ*, 684, 1390
Richer, H. B. et al., 2008, *AJ*, 135, 2141
Rocha-Pinto, H. J., Scalo, J., Maciel, W. J., & Flynn, C., 2000, *ApJL*, 531, L115
Russell, H. N., 1913, *The Observatory*, 36, 324
—, 1914, *The Observatory*, 37, 165
Rutledge, R. E., Basri, G., Martín, E. L., & Bildsten, L., 2000, *ApJL*, 538, L141
Sandage, A., 1993, *AJ*, 106, 687
Scargle, J. D., 1982, *ApJ*, 263, 835
Schmidt, S. J., Cruz, K. L., Bongiorno, B. J., Liebert, J., & Reid, I. N., 2007, *AJ*, 133, 2258
Sesar, B., Ivezić, Ž., & Jurić, M., 2008, *ApJ*, 689, 1244
Skrutskie, M. F. et al., 2006, *AJ*, 131, 1163
Skumanich, A., 1972, *ApJ*, 171, 565
Smecker-Hane, T. A., Cole, A. A., Gallagher, III, J. S., & Stetson, P. B., 2002, *ApJ*, 566, 239

Soderblom, D. R., Duncan, D. K., & Johnson, D. R. H., 1991, *ApJ*, 375, 722
Somerville, R. S., & Primack, J. R., 1999, *MNRAS*, 310, 1087
Stassun, K. G., Hebb, L., López-Morales, M., & Prša, A., 2009, IAU Symposium, Vol. 258, Eclipsing binary stars as tests of stellar evolutionary models and stellar ages, E. E. Mamajek, D. R. Soderblom, & R. F. G. Wyse, eds. pp. 161–170
Stassun, K. G., Mathieu, R. D., & Valenti, J. A., 2006, *Nature*, 440, 311
—, 2007, *ApJ*, 664, 1154
Stassun, K. G., Mathieu, R. D., Vaz, L. P. R., Stroud, N., & Vrba, F. J., 2004, *ApJS*, 151, 357
Tolstoy, E., & Saha, A., 1996, *ApJ*, 462, 672
Torres, S., García-Berro, E., Isern, J., & Figueras, F., 2005, *MNRAS*, 360, 1381
Twarog, B. A., 1980, *ApJ*, 242, 242
van den Bergh, S., 1993, *MNRAS*, 262, 588
van den Bergh, S., & Tammann, G. A., 1991, *ARAA*, 29, 363
van der Marel, R. P., 2001, *AJ*, 122, 1827
Vandenberg, D. A., Stetson, P. B., & Bolte, M., 1996, *ARAA*, 34, 461
Vergely, J.-L., Köppen, J., Egret, D., & Bienaymé, O., 2002, *A&A*, 390, 917
Weinberg, M. D., 2000, *ApJ*, 532, 922
Weinberg, M. D., & Nikolaev, S., 2001, *ApJ*, 548, 712
West, A. A., Hawley, S. L., Bochanski, J. J., Covey, K. R., Reid, I. N., Dhital, S., Hilton, E. J., & Masuda, M., 2008, *AJ*, 135, 785
West, A. A. et al., 2004, *AJ*, 128, 426
Whitney, B. A. et al., 2008, *AJ*, 136, 18
Williams, B. F., 2003, *AJ*, 126, 1312
Wilson, R. E., & Devinney, E. J., 1971, *ApJ*, 166, 605
Yanny, B. et al., 2003, *ApJ*, 588, 824
York, D. G. et al., 2000, *AJ*, 120, 1579
Zaritsky, D., Harris, J., Thompson, I. B., & Grebel, E. K., 2004, *AJ*, 128, 1606